BBA - Molecular Basis of Disease 1866 (2020) 165900

Contents lists available at ScienceDirect

BBA - Molecular Basis of Disease

journal homepage: www.elsevier.com/locate/bbadis

Longitudinal study of *Pex1*-G844D NMRI mouse model: A robust pre-clinical model for mild Zellweger spectrum disorder

Tanguy Demaret[a,*], Martin Roumain[b], Jérôme Ambroise[c], Jonathan Evraerts[a], Joachim Ravau[a], Caroline Bouzin[d], Bertrand Bearzatto[c], Jean-Luc Gala[c], Hedwig Stepman[e], Sandrine Marie[f], Marie-Françoise Vincent[f], Giulio G. Muccioli[b], Mustapha Najimi[a], Etienne M. Sokal[a]

[a] *Laboratoire d'Hépatologie Pédiatrique et Thérapie Cellulaire, Unité PEDI, Institut de Recherche Expérimentale et Clinique (IREC), Université Catholique de Louvain (UCLouvain), 1200 Brussels, Belgium*
[b] *Bioanalysis and Pharmacology of Bioactive Lipids Research Group (BPBL), Louvain Drug Research Institute (LDRI), Université Catholique de Louvain (UCLouvain), 1200 Brussels, Belgium*
[c] *Center for Applied Molecular Technologies (CTMA), Institut de Recherche Expérimentale et Clinique (IREC), Université Catholique de Louvain (UCLouvain), 1200 Brussels, Belgium*
[d] *IREC Imaging Platform (2IP), Institut de Recherche Expérimentale et Clinique (IREC), Université Catholique de Louvain (UCLouvain), 1200 Brussels, Belgium*
[e] *Department of Laboratory Medicine, Ghent University Hospital, 9000 Ghent, Belgium*
[f] *Department of Laboratory Medicine, Cliniques Universitaires Saint-Luc, Université Catholique de Louvain (UCLouvain), 1200 Brussels, Belgium*

ARTICLE INFO

Keywords:
Peroxisome biogenesis disorder
Oxysterol
Very long-chain fatty acid
Intra-hepatic cholestasis
PEX1 p.Gly843Asp
PEX1 c.2528G > A

ABSTRACT

Zellweger spectrum disorders (ZSD) are inborn errors of metabolism caused by mutations in *PEX* genes that lead to peroxisomal biogenesis disorder (PBD). No validated treatment is able to modify the dismal progression of the disease. ZSD mouse models used to develop therapeutic approaches are limited by poor survival and breeding restrictions. To overcome these limitations, we backcrossed the hypomorphic *Pex1* p.G844D allele to NMRI background. NMRI mouse breeding restored an autosomal recessive Mendelian inheritance pattern and delivered twice larger litters. Mice were longitudinally phenotyped up to 6 months of age to make this model suitable for therapeutic interventions. ZSD mice exhibited growth retardation and relative hepatomegaly associated to progressive hepatocyte hypertrophy. Biochemical studies associated with RNA sequencing deciphered ZSD liver glycogen metabolism alterations. Affected fibroblasts displayed classical immunofluorescence pattern and biochemical alterations associated with PBD. Plasma and liver showed very long-chain fatty acids, specific oxysterols and C_{27} bile acids intermediates elevation in ZSD mice along with a specific urine organic acid profile. With ageing, C_{26} fatty acid and phytanic acid levels tended to normalize in ZSD mice, as described in patients reaching adulthood. In conclusion, our mouse model recapitulates a mild ZSD phenotype and is suitable for liver-targeted therapies evaluation.

Abbreviations: 7-OHC, 7-hydroxycholesterol; 7α-OHCnone, 7α-hydroxy-4-cholesten-3-one; BA, bile acids; BCFA, branched-chain fatty acids; C_{22}, docosanoic acid; C_{24}, tetracosanoic acid; C_{26}, hexacosanoic acid; C26LPC, $C_{26:0}$lysophosphatidylcholine; DAPI, 4′,6-diamidino-2-phenylindole; DMA, dimethyl acetal; eGFP-PTS1, green fluorescent protein linked to peroxisome targeting signal 1; FDR, false discovery rate; G6Pase, glucose-6-phosphatase; gDNA, genomic DNA; gGT, gamma-glutamyltransferase; GPT, glutamate-pyruvate transaminase; HNF4α, hepatocyte nuclear factor 4 alpha; MEF, mouse embryonic fibroblasts; MS, mass spectrometer; NGS, normal goat serum; NMRI, Naval Medical Research Institute; ORO, Oil Red O; PAS, Periodic-acid Schiff; PBD, peroxisomal biogenesis disorder; PMP70, 70-kDa peroxisomal membrane protein; PPARα, peroxisome proliferator-activated receptor alpha; RNA-seq, RNA sequencing; SR, Sirius red; TBS, tris-buffered saline; VLCFA, very long-chain fatty acids; WGA, wheat germ agglutinin; ZSD, Zellweger spectrum disorders

* Corresponding author.
E-mail addresses: tanguy.demaret@uclouvain.be (T. Demaret), martin.roumain@uclouvain.be (M. Roumain), jerome.ambroise@uclouvain.be (J. Ambroise), jonathan.evraerts@uclouvain.be (J. Evraerts), joachim.ravau@uclouvain.be (J. Ravau), caroline.bouzin@uclouvain.be (C. Bouzin), bertrand.bearzatto@uclouvain.be (B. Bearzatto), jean-luc.gala@uclouvain.be (J.-L. Gala), hedwig.stepman@uzgent.be (H. Stepman), sandrine.marie@uclouvain.be (S. Marie), marie-francoise.vincent@uclouvain.be (M.-F. Vincent), giulio.muccioli@uclouvain.be (G.G. Muccioli), mustapha.najimi@uclouvain.be (M. Najimi), etienne.sokal@uclouvain.be (E.M. Sokal).

https://doi.org/10.1016/j.bbadis.2020.165900
Received 10 April 2020; Received in revised form 27 June 2020; Accepted 15 July 2020
Available online 18 July 2020

1. Introduction

Zellweger spectrum disorders (ZSD) are autosomal recessive disorders affecting 1 in 90,000 births [1]. ZSD are caused by genetic alterations in *PEX* genes which lead to peroxisome biogenesis disorder (PBD) [2]. Severely affected patients present in the neonatal period with severe hypotonia, craniofacial dysmorphism, hepatic dysfunction and failure to thrive, and they will eventually die of liver insufficiency during their first year of life (former Zellweger syndrome) [3]. Reversible neonatal cholestasis is a milder form of the disease (former infantile Refsum disease) with part of the patients that survive into adulthood with, however, developmental delay, vision and/or hearing impairment and progressive leukodystrophy [4]. Since newborn screening implementation for X-linked adrenoleukodystrophy, a related peroxisomal disorder, neonatal diagnosis of ZSD is rendered possible, mostly in the United States, by $C_{26:0}$lysophosphatidylcholine (C26LPC) quantification on dried blood spot [5]. ZSD diagnosis is ascertained by biochemical studies on plasma, erythrocytes, patient's skin fibroblasts, and/or urine. Classically, plasma branched-chain fatty acids (BCFA) phytanic and pristanic acids, very long-chain fatty acids (VLCFA), C_{27} bile acids (BA) intermediates (di- and trihydroxycholestanoic acids) and pipecolic acid levels are elevated. Erythrocytes plasmalogen are synthetized within peroxisomes and their levels are decreased only in severe ZSD patients [6]. Analysis on patient's cells allows similar metabolites quantification along with enzymatic analysis and peroxisome immunofluorescence studies [7]. Some authors report a relatively specific urine organic acid profile in ZSD patients [8,9]. Finally, next generation sequencing of all *PEX* genes related to ZSD confirms the diagnosis [10]. To date, standard of care is supportive since no intervention is validated in clinical practice [11]. In a research setting, we performed the first pediatric hepatocyte transplantation in Europe in a 4-year-old girl affected by a mild ZSD and we achieved biochemical success [12]. After that, we reported bio-clinical benefits obtained by living-donor liver transplantation in 3 mild ZSD patients [13,14].

Based on this experience in mild ZSD patients, pre-clinical studies are required to validate these liver-targeted therapies (*i.e.* hepatocyte and liver transplantation). ZSD mouse models are useful to study PBD pathophysiology and to evaluate therapeutic approaches [15]. Mouse models with generalized *Pex* gene deletion suffer from neonatal death impairing post-natal longitudinal studies and therapeutic intervention [16–18]. Conditional *Pex* gene KO was developed to overcome these limitations. Hepatocyte *Pex5* deletion was carried out to study liver carbohydrate metabolism alterations caused by PBD, but this artificial condition does not clinically recapitulate liver glycogen alterations (*i.e.* ZSD mice resist to fast) [19]. *Pex1* p.G844D mouse model (hereafter called *Pex1*-G844D) was developed as a murine equivalent to the hypomorphic *PEX1* p.G843D human allele conferring a milder phenotype to ZSD patients [20]. *Pex1*-G844D allele was inserted in a pure C57BL/6N background and leads to a relatively severe ZSD phenotype with 20% survival at 1 month [21]. A second *Pex1*-G844D mouse model was created in a mixed 129/SvEv and C57BL/6N background [22]. This model exhibits a restricted survival rate of 59% at 1 month along with progressive retinal degeneration [23]. No robust longitudinal (> 15 days) biochemical study was carried out on ZSD mouse models, partly due to their restricted survival rate.

To set up a ZSD mouse model suitable for evaluation of liver-directed therapies, we backcrossed *Pex1*-G844D allele in Naval Medical Research Institute (NMRI) background known for its robustness and for delivering large litters. NMRI mice homozygous for *Pex1*-G844D mutation reached 78% survival rate at 1 month while keeping a ZSD phenotype composed of growth retardation, hepatomegaly, chronic liver injury, cholestasis, and classical biochemical alterations associated with ZSD. We report for the first time in a ZSD mouse model that several disease markers tend to normalize with ageing, as reported for ZSD patients surviving into adulthood [4] and that urine organic acids profile is similar to that of ZSD patients [8]. Liver RNA sequencing (RNA-seq) highlighted multiple pathway modulations associated with ZSD. These data make NMRI ZSD mice a robust mouse model to evaluate liver-targeted therapies for ZSD.

2. Methods

2.1. Mice care and breeding

Mice were bred in a specific-pathogen-free environment in individually ventilated cages with 12 h light/12 h dark cycle. Mice had unrestricted access to food (Carfil, Mice Breeding diet) and water. No gel food was needed to wean pups at 4 weeks contrary to Hiebler et al. [22]. Mice and food were weighted once a week to evaluate growth and food consumption. All experiments were carried out in accordance with the EU Directive 2010/63/EU for animal experiments and approved by the Ethical Committee for Animal Experimentation at the Health Science Sector, UCLouvain, Brussels, Belgium (2017/UCL/MD/006).

2.2. Pex1-G844D NMRI mice generation and genotyping

Two males and 4 females C57BL/6N mice aged of 4 weeks and heterozygous for the *Pex1*-G844D allele were bought from The Jackson Laboratory (MMRRC stock #37405) [22]. One ten-week-old female NMRI mouse from Charles River Laboratories (Sulzfeld, Deutschland) was used to backcross the *Pex1*-G844D allele for three generations leading to a mixed background (87.5% NMRI, 12.5% C57BL/6N). Inbreeding of the F3 was performed to characterize the mouse model. Litters genotyping was achieved by genomic DNA (gDNA) extraction from 1 mm tail snips following fast, cheap and straightforward HotSHOT DNA extraction protocol [24]. PCR (Promega, M7401) was run on gDNA following manufacturer's instructions, for 45 cycles, with the following forward 5′-TCCCTGCTCACTTCRGGAC-3′ and reverse primer 5′-TAGGCAAGCTCTTTATCACC-3′ (annealing temperature: 54 °C) in a PCR mix containing $MgCl_2$ and deoxynucleotides (Promega, U1511) at a final concentration of 1 mM and 0.2 mM, respectively. PCR products were run on a 1% agarose gel (UltraPure Agarose, Invitrogen, 15510-027) containing intercalating agent diluted 1/20000 (Midori Green Advance DNA Stain, Nippon Genetics, MG04) at 120 V for 45 min. WT and *Pex1*-G844D alleles yielded 230- and 407-bp products, respectively (Fig. 1A). NMRI *Pex1*-G844D cryopreserved embryos are available for collaboration.

2.3. Blood, urine and organs collection

Mice euthanasia and samples collection were performed in the morning on fed mice. Mice were anesthetized by intraperitoneal injection (2 μL/g of body weight) with the following anesthetic solution: ketamine 100 mg/mL (Nimatek, Eurovet), xylazine 20 mg/mL (Rompun, Bayer), and NaCl 0.9% (Mini-Plasco NaCl 0.9%, B-Braun) in a volume ratio of 2/1/1 (final ketamine and xylazine concentration: 100 mg/kg and 10 mg/kg, respectively). Abdominal cavity was open by transverse laparotomy and blood was drawn from the inferior vena cava through 27G needle (Microlance 3, BD) in heparinized syringe (Portex Arterial Blood Sampling Syringe, Smiths Medical, 4041E). A drop of total blood was disposed on Guthrie card then total blood was centrifuged 15 min at 1.500 *g* and 4 °C. Plasma was aliquoted and erythrocytes were washed twice in NaCl 0.9% and stored in butylated hydroxytoluene (Sigma, B1378) coated polypropylene microtubes. After blood collection, mice were killed by cervical dislocation and liver was collected, weighted and sampled following lobar segmentation [25]. Left lateral lobe was fixed in formaldehyde 4% (VWR, 11699408) overnight and embedded in paraffin or in Tissue-Tek O.C.T. (Sakura, 4583), respectively. Left medial lobe and right lateral lobe were weighted in lysing matrix tubes (Lysing Matrix D, MP Bio, 116,913,100), snap frozen in liquid nitrogen and stored at −80 °C. To collect urine samples, 2-month-old mice were individually placed in

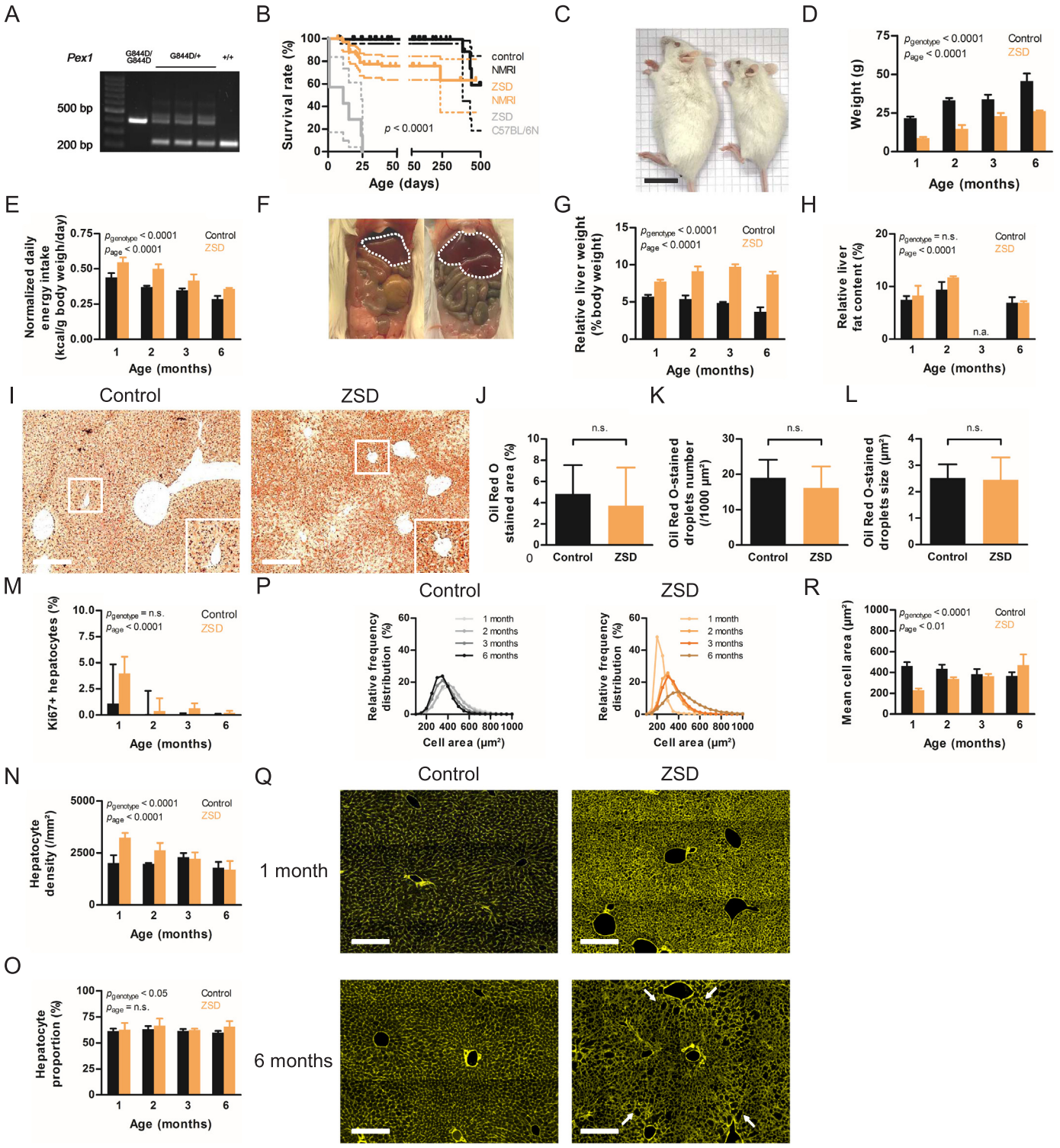

(caption on next page)

mouse metabolic cages (UNO, 100100007) for 24 h. Urine was centrifuged at 1500*g* for 5 min at 4 °C and supernatant was snap frozen in liquid nitrogen and stored at −80 °C.

2.4. Histological analyses

2.4.1. H&E, PAS, SR and ORO staining, imaging and quantification

Formalin-fixed paraffin-embedded left lateral liver lobes were cut into 5 µm sections and processed for H&E, Periodic-acid Schiff (PAS) without and with prior saliva treatment and Sirius red (SR) staining. Slides were stained in one same batch to avoid inter-batches variations. Formalin-fixed sucrose impregnated Tissue-Tek O.C.T. embedded liver lobes were cut on a cryostat (Thermo Fisher Scientific Microm, HM 560) into 10 µm - section and processed for Oil Red O (ORO) staining. Slides were digitalized at 20× using a slide scanner (Leica Biosystems, SCN400). Tissue was manually delineated and TissueIA (Leica Biosystems) "Measure Stained Area" algorithm was used to quantify PAS and SR stained area as a proxy for glycogen and collagen liver

Fig. 1. Zellweger spectrum disorder (ZSD) mice exhibited reduced survival rate, growth retardation with higher energy intake, and relative hepatomegaly associated to progressive hepatocyte hypertrophy. (A) Genotyping gel from five 3-week-old pups. The product size difference is a consequence of 177 bp residual *Neo* cassette fragment in an intron near the *Pex1*-G844D allele [22]. (B) Survival curves from control mice (black curve, $n = 223$), ZSD mice in Naval Medical Research Institute (NMRI, orange curve, $n = 68$) and C57BL/6N (grey curve, $n = 7$) backgrounds. NMRI ZSD mice showed increased survival compared to C57BL/6N ZSD mice. All the data reported hereafter were collected from the NMRI background. Log-rank test, dashed lines represent 95% confidence interval. (C) Control (left) and ZSD (right) mouse at 2 months highlighted a significant growth retardation in ZSD mouse. Scale bar: 2 cm. (D) Mouse weight longitudinal study confirmed the significant growth retardation in ZSD mice with no catch up growth detectable. (E) Daily energy intake normalized for body weight disclosed a higher energy intake in ZSD mice. Thus, energy intake did not explain growth retardation detected in ZSD mice. (F) Control (left) and ZSD (right) mouse abdominal cavity at 3 months exposed an enlarged liver in ZSD mouse. (G) Mouse liver weight longitudinal analysis revealed a relative hepatomegaly which progressively increased in ZSD mice ($p_{interaction} < 0.0001$). (H) Liver fat content quantification did not highlight any difference between ZSD and control liver and thus ruled out liver lipid deposition as a cause to the relative hepatomegaly in ZSD mice. (I) Liver Oil Red O staining showed hepatocytes lipid droplets in both genotypes. Droplets deposition zonation favoring periportal space was perceptible in ZSD mice liver. Inserts show higher magnification of the boxed area. Scale bar: 200 μm. Liver Oil Red O (J) - stained area (%), (K) - stained droplets number (/1000 μm^2) and (L) -stained droplets size (μm^2) digital quantification did not detect difference between ZSD and control livers. Pigment precipitation (black dots) was excluded during digital quantification. Longitudinal study on liver slides stained for hepatocyte nuclear factor 4 alpha (hepatocyte marker) and Ki67 (proliferation marker) to measure (M) proportion of proliferative hepatocytes, (N) hepatocyte density (/mm^2), (O) hepatocyte proportion relative to total liver cells. ZSD hepatocytes did not show any significant proliferation increase. Yet, compared to control, the ZSD hepatocyte density was higher at one month and slowly decreased to control levels afterwards. This suggested that hepatocyte proliferation took place before 1 month of age, followed by hepatocyte hypertrophy, in ZSD mice. (P) Longitudinal study of liver cell area relative distribution based on wheat germ agglutinin-rhodamine staining (WGA, cell membrane marker) highlighted a progressive trend to liver cell area increase in ZSD. (Q) WGA-stained liver slides depicted smaller hepatocytes in 1-month-old ZSD liver compared to control. At 6 months, ZSD liver slides presented enlarged cells with a zonation favoring the perivenular region (white arrows). Scale bar: 200 μm. (R) Longitudinal mean liver cell area quantification underlined a reduced ZSD liver cell area at 1 month of age followed by a progressive cell enlargement exceeding control liver cell area at 6 months. Two-way ANOVA and $n = 6$/timepoint/genotype (longitudinal) or Mann-Whitney test and $n \geq 5$/group (2 groups), median ± interquartile range, n.a.: not available, n.s.: not significant.

content, respectively. ORO stained area and characteristics were analyzed with Visiopharm (v2017.2) to quantify total lipid droplets surface, lipid droplets number, and mean lipid droplets area.

2.4.2. Glucose-6-phosphatase activity

2-month-old mice left lateral liver lobes Tissue-Tek O.C.T. embedded in Tissue-Tek Cryomold (Sakura, 4557) were cut on a cryostat (Thermo Fisher Scientific Microm, HM 560) into 10 μm section and processed for glucose-6-phosphatase (G6Pase) activity staining as described elsewhere [26]. Slides were mounted with aqueous mounting medium (Dako, S3025) and digitalized at 20× using a slide scanner (Leica Biosystems, SCN400). Tissue was manually delineated with Visiopharm (v2017.2) and processed for G6Pase stained area quantification.

2.4.3. Fluorescent staining

Formalin-fixed paraffin-embedded left lateral liver lobes were cut into 5 μm section, deparaffinized and rehydrated.

2.4.3.1. Peroxisomal membrane protein. Slides were immersed in Target Retrieval Solution (Dako, S1699) for 30 min at 100 °C and rinsed three times in PBS (Gibco, 18912-014). Non-specific immunostaining was prevented by 5% normal goat serum (NGS, Sigma, G9023) in PBS (v/v) incubation for 1 h at RT. Slides were incubated with anti-70-kDa peroxisomal membrane protein (PMP70) antibody (Abcam, ab85550, lot GR99621-1, 1/1000) in 0.5% NGS overnight at 4 °C. Slides were rinsed three times with PBS and incubated with Alexa Fluor 594 anti-rabbit antibody (Thermo Fischer Scientific, A11012, 1/500) in 0.5% NGS for 1 h at RT. Slides were rinsed three times with PBS, nuclei were stained with 4′,6-diamidino-2-phenylindole (DAPI, Sigma, D9542) and slides were mounted with fluorescence mounting medium (Dako, S3023).

2.4.3.2. Hepatocytes and proliferative nuclei. Endogenous peroxidases were inhibited 20 min with 3% hydrogen peroxide in methanol. Sections were then subjected to antigen retrieval in 10 mM citrate buffer pH 5.7 and microwaved for 5 min at 900 W and 15 min at 90 W followed by aspecific antigen binding sites blocking in bovine serum albumin 5% + Tween20 0,1% in tris-buffered saline (TBS). Slides were incubated in anti-Ki67 primary antibody (CellSignaling, 12,202, lot 5, 1/100) for 1 h30 at RT. This was followed by an incubation with anti-rabbit antibody (Dako, K4003) for 40 min at RT. This reaction was visualized using Alexa Fluor 488-conjugated tyramide (Thermo Fisher Scientific, B40953, dilution 1/200). Hepatocyte nuclear factor 4 alpha (HNF4α) immunostaining was performed after a new citrate buffer incubation step, using anti-HNF4α antibody (Perseus Proteomics, PPH141500, lot A2, 1/200), anti-mouse antibody (Dako, K4001) and Alexa Fluor 647-conjugated tyramide (Thermo Fisher Scientific, B40958). After a washing step, nuclei were finally stained with Hoechst33342 (Sigma, 14533) and slides were mounted with fluorescent mounting medium.

2.4.3.3. Cell membranes. Slides were immersed in 10 mM citrate buffer pH 5.7, microwaved for 5 min at 900 W and 15 min at 90 W and then rinsed once in distilled water and once in Tween20 0.1% in TBS. To stain cell membranes, slides were incubated with wheat germ agglutinin-rhodamine (WGA, Vector, RL-1022, lot ZF0717, 1/50) in PBS for 2 h at RT. Slides were rinsed three times in Tween20 0.1% in TBS and nuclei were counterstained with Hoechst33342. After washing twice in Tween20 0.1% in TBS and once in distilled water, slides were mounted with fluorescence mounting medium.

2.4.3.4. Imaging and quantification. PMP70-stained slides were imaged on a Cell Observer Spinning Disk confocal microscope (Zeiss) using a Plan Apochromat 100×/1.4 Oil DICII objective.

HNF4α-Ki67-stained and WGA-stained slides were digitalized using a Pannoramic 250 FlashIII scanner (3DHistech) at 20× magnification. Scanned slides were then analyzed using Visiopharm (v2017.2). A 5.5 × 5.5 mm region of interest was delineated manually on each tissue sections at low magnification and large empty spaces (lumens of macro vessels) were automatically discarded. Cells were detected at high resolution (20×) with a cell shape-based or nuclear-based cell classification relying on the WGA or Hoechst staining, respectively. Following segmentation, post processing steps were applied to measure WGA cell area or to separate HNF4α+/− and Ki67+/− cells. The same parameters were kept constant for all slides.

2.5. RNA-seq

Two-month-old mice right lateral liver lobes were placed into 2.0-ml Lysing Matrix D tubes (MP Bio, 116,913,100) and homogenized by mechanical grinding for 2 × 40 s at 6,0 m/s on the FastPrep system (MP Biomedicals). After guanidinium thiocyanate-phenol-chloroform extraction, RNA was further extracted on column (RNeasy, QIAGEN, 74104) and treated with DNase (DNAse-set, QIAGEN, 79254) to reduce gDNA contamination. In total, RNA from 12 samples were quantified by

Qubit RNA BR assay kit (Thermo Fisher Scientific, Q10211) on a Qubit 4 Fluorometer (Thermo Fisher Scientific). RNA integrity was evaluated on the Agilent 2100 Bioanalyzer using the RNA 6000 nano kit (Agilent, 5067-1511). All samples had RNA integrity number values ≥7.8. Libraries were prepared starting from 150 ng of total RNA using the KAPA RNA HyperPrep Kit with RiboErase (KAPA Biosystems, KK8560) following the manufacturer's recommendations (KR1351 – v1.16). Libraries were equimolarly pooled and sequenced on a single lane on an Illumina NovaSeq 6000 platform. All libraries were paired-end (2 × 100 bp reads) sequenced and a minimum of 25 million paired-end reads were generated per sample. All sequencing data were analyzed using the Automated Reproducible MOdular workflow for preprocessing and differential analysis of RNA-seq data (ARMOR) pipeline [27]. In parallel, estimated transcript abundances were analyzed for differential gene expression with edgeR in order to compute the modulation (*i.e.*, the fold change): ZSD *versus* control mice liver [28]. Raw *p*-values were adjusted for multiple testing using Benjamini Hochberg method and a false discovery rate (FDR) < 0.05 was considered significant. Over-representation analysis were conducted from the resulting list of highly significantly (FDR < 0.01) modulated genes on Gene Ontolgoy (GO), Kyoto Encyclopedia of Gene and Genomes (KEGG), and Reactome Pathway database, using the limma and ReactomePA Bioconductor packages. In addition, Reactome pathways for *Homo sapiens* glucose and glycogen metabolism (R-HSA-70326, R-HSA-70171, R-HSA-70263, R-HSA-8982491) were manually analyzed for mouse orthologs. If one gene had several isoforms, the non-liver isoforms were discarded. Cholangiocytes markers [29,30], liver collagen genes [31], peroxisome proliferator-activated receptor alpha (PPARα) target genes [19,21,32] and hepatocytes proliferation genes [33] were collected from literature. Gene set enrichment of these pathways were shown as barcode plot in which genes were ranked according to the modulation (*i.e.*, the $\log_2$ (fold change)) induced by the disease status. In addition, modulation of significantly modulated genes in *Pex5* mouse hepatocytes conditional KO mouse model reported by Peeters et al. were correlated to our data [19]. Raw and processed RNA-seq data were deposited and made publicly available on the Gene Expression Omnibus (GSE145524).

2.6. MEF collection and characterization

Mouse embryonic fibroblasts (MEF) were collected from WT and ZSD mouse embryos and cultured as described elsewhere [34]. Cells were collected between passage 4 and 10. Two million MEF by sample were collected in radioimmunoprecipitation assay buffer (150 mM sodium chloride (Sigma, 746,398), 50 mM Tris-base pH 8 (Sigma, T6066), 1% v/v IGEPAL CA-630 (Sigma, I3021), 0.5% w/v sodium deoxycholate (Sigma, D6750), 0.1% w/v sodium dodecyl sulfate (Acros Organics, 226,145,000)) and stored at −80 °C before analysis. Cell protein content was quantified for normalization purposes (Pierce BCA Protein Assay Kit, Thermo Fisher Scientific, 23227). MEF were immuno-labelled for catalase, a peroxisome lumen enzyme, and PMP70 to highlight PBD, as described previously [34]. MEF peroxisome biogenesis was further evaluated through lentiviral expression of a green fluorescent protein linked to peroxisome targeting signal 1 (eGFP-PTS1), as described elsewhere [34]. Nuclei were stained with DAPI and cells were imaged on a cell observer spinning disk confocal microscope (Zeiss) using a Plan Apochromat 100×/1.4 Oil DICII objective.

2.7. Biochemical analyses

2.7.1. Glycemia & fasting

Blood drop was collected from the tail vein and morning glycemia (8 AM) was measured using glucometer (FreeStyle Precision Neo, Abbott). To evaluate glycemic response to fast, mice were placed in a clean cage without food access for 6 h (from 8 AM to 2 PM) after what glycemia was controlled.

2.7.2. Total lipids quantification

Total lipids were extracted in methanol-chloroform from about 100 mg liver lobe homogenized in distilled water (Baxter, AKF7114), and quantified as described here [35]. Lipid content was normalized to liver weight.

2.7.3. Protein quantification

Protein content of liver homogenates in distilled water was quantified using Pierce BCA Protein Assay Kit (Thermo Fisher Scientific, 23227) according to manufacturer's instructions. Protein content was normalized to liver weight.

2.7.4. Glycogen quantification

Liver glycogen content was measured following a protocol modified from [36,37]. Briefly, left medial liver lobes were homogenized in lysing matrix tubes in distilled water. About 10 mg of liver were digested in acidic solution for 1 h at 100 °C. Digested solution was neutralized and glucose was quantified using a glucometer (FreeStyle Precision Neo, Abbott). A conversion factor of 0.9 was used to convert glucose to glycogen [38]. Glycogen was normalized to liver weight.

2.7.5. Urine organic acids quantification

Urine organic acids were quantified with a clinically validated method using a gas chromatograph (Hewlett-Packard, 6890 Series) equipped with a CP-Sil 8CB capillary column (Agilent Technologies, CP8751) coupled to a mass spectrometer (MS) (Hewlett-Packard, 5973 Mass Selective Detector). Pentadecanoic acid was used as internal standard and quantification was normalized to urine creatinine.

2.7.6. Plasma clinical biology tests

Plasma alkaline phosphatases activity, gamma-glutamyltransferases (gGT) activity, glutamate-oxaloacetate transaminase activity, glutamate-pyruvate transaminase (GPT) activity, total cholesterol, albumin and total bilirubin were quantified on plasma samples with a dry chemistry system (Fuji DRI-CHEM NX500, Fujifilm).

2.7.7. Erythrocyte plasmalogen quantification

Erythrocyte plasmalogens were derivatized in methanolic HCl 3 M (Sigma, 33050 U) for 4 h at 90 °C, extracted in hexane (Biosolve, 082906) and quantified using a gas chromatograph (Agilent Technologies, 6890N) equipped with a HP-5MS capillary column (Agilent Technologies, 19091S-433) and coupled to a MS (Agilent Technologies, 5973N). $C_{17:0}$ (Sigma, H3500) was used as internal standard, and $C_{16:0}$ and $C_{18:0}$ dimethyl acetals (DMA) (Avanti Polar Lipids, 852,446 and 852,448) and $C_{16:0}$ and $C_{18:0}$ (Sigma, P5585 and S4751) as calibration standards. Results are expressed as $C_{16:0}$ DMA/$C_{16:0}$ and $C_{18:0}$ DMA/$C_{18:0}$ ratios.

2.7.8. Pipecolic acid quantification

Pipecolic acid was quantified without derivatization by ultra-high performance liquid chromatography (1290 infinity LC, Agilent Technologies) equipped with Acquity UPLC HSS T3 column (Waters, 186,003,539) coupled to MS/MS (6460 Triple Quad Mass Spectrometer, Agilent Technologies, K6460). DL-2-piperidine-d_9-carboxylic acid (CDN isotopes, D5087) was used as internal standard. δ1-pipéridéine-6-carboxylate (synthetized as described elsewhere [39]) and pipecolic acid (Sigma, P2519) were used as calibration standards.

2.7.9. C26LPC quantification

Six millimeters diameter punches were cut from saturated area of dried blood spot. Punches were then immersed in glass vials containing $C_{17:0}$lysophosphatidylcholine as internal standard and chloroform (8 mL), methanol (4 mL), water (2 mL) and HCl (300 μL, 2 M). Samples were next centrifuged after mixing and sonicating, organic phase was recovered and dried under a nitrogen steam. Organic residue was re-suspended and pre-purified by solid phase extraction. C26LPC from the

eluate was analyzed by HPLC-MS/MS using a Xevo TQ-S MS (Waters) coupled to an Acquity UPLC Class H (Waters). Analyte separation was performed using a Kinetex C18 HPLC column (5 μm, 150 × 4.6 mm, Phenomenex). Mobile phase was a gradient of methanol, acetonitrile and water containing ammonium acetate. MS analysis was performed using an electrospray ionization source in the positive mode.

2.7.10. BCFA and VLCFA quantification

The BCFA phytanic and pristanic acids, and the VLCFA docosanoic acid (C_{22}), tetracosanoic acid (C_{24}) and hexacosanoic acid (C_{26}) were quantified with a clinically validated method using a gas chromatograph equipped with a CP-Sil 8CB capillary column (Agilent Technologies, CP8751) and coupled to a MS (TRACE 1310 Mainframe MS, Thermo Fisher Scientific, 14800402). Deuterated and non-deuterated phytanic and pristanic acids and C_{22}, C_{24} and C_{26} were used as internal standards and calibration standards, respectively.

2.7.11. Oxysterols and bile acids quantification

Oxysterols were analyzed using a validated HPLC-MS method [40].

BA were analyzed using another validated method adapted from [41]. Samples (plasma or liver homogenates) were placed in acetone containing deuterated internal standards to allow for protein precipitation overnight. Samples were then centrifuged, supernatant recovered and evaporated to dryness. The resulting residue was resuspended and injected in the HPLC-MS system consisting of an LTQ-Orbitrap XL MS (Thermo Fisher Scientific) coupled to an Accela HPLC system (Thermo Fisher Scientific). Analyte separation was performed on an Ascentis Express C-18 column (2.7 μm, 150 × 4.6 mm) (Sigma-Aldrich). Mobile phase was a gradient of acetonitrile and water containing formic acid. MS analysis was performed using an electrospray ionization source in the negative mode. Calibration curves were prepared in the same conditions. Bile acid species were grouped according to their family (Supplementary Table 1). BA plasma-liver ratios were calculated, and reported when different from 0 or ∞.

2.8. General statistical analysis and artwork

Log-rank test, two-tailed Mann-Whitney tests with confidence intervals of 95%, two-way ANOVA and Spearman's correlation were performed using GraphPad Prism v5.02 for Windows (GraphPad Software). p-Values < 0.05 were considered significant. Chi-squared tests were performed with Statistical Package for the Social Sciences v24 (SPSS Statistics, I.B.M.) to assess sex ratios and genotypes imbalance. Publisher (Office 365, Microsoft) was used to draw the figures.

3. Results

3.1. Pex1-G844D backcrossing in NMRI background eased the breeding and restored autosomal recessive Mendelian inheritance pattern

Breeding of *Pex1*$^{G844D/+}$ C57BL/6N mice lead to 52 pups (among 12 litters, mean: 4.3 pups/litter), 7 pups (13.5%) were ZSD mice (*Pex1*$^{G844D/G844D}$) compared to 25% predicted by the Mendelian inheritance. None of the C57BL/6N homozygous pups survived more than 25 days (Fig. 1B). To get larger litters and pups more robust, we backcrossed the *Pex1*-G844D allele in NMRI background for 3 generations. *Pex1*$^{G844D/+}$ NMRI mice were bred and gave birth to 291 pups among 29 litters (mean: 10 pups/litter, p-value < 0.0001 *versus* C57BL/6N breeding). With this strain, we obtained an inheritance pattern that followed the Mendelian inheritance pattern for an autosomal recessive disorder: 77 *Pex1*$^{+/+}$ (26.5%), 146 *Pex1*$^{G844D/+}$ (50.2%) and 68 *Pex1*$^{G844D/G844D}$ (23.4%) (p-value > 0.05). This meant that all genotypes survived until birth. *Pex1*$^{+/+}$ and *Pex1*$^{G844D/+}$ exhibited a similar phenotype and were used as control for ZSD mice (*Pex1*$^{G844D/G844D}$). The male/female ratio was 1:1 in control mice and 1.16:1 in ZSD mice (p-value > 0.05), meaning that genotype did not alter the 1:1 expected sex ratio. Of note, female ZSD mice were sterile, male ZSD mice were fertile but they were not used for breeding. All the data reported hereafter were collected from our *Pex1*-G844D NMRI mice strain delivering large litters and robust ZSD pups.

3.2. ZSD mice presented growth retardation and relative hepatomegaly associated to progressive hepatocyte hypertrophy

ZSD mice presented a reduced survival rate compared to control mice (p-value < 0.0001, Fig. 1B). The first month of life was a critical period during which 22% of ZSD mice died. After weaning, none except one ZSD mice died prematurely, however they exhibited severe growth retardation. This phenotype was already evident at day 3 and was maintained until death (Fig. 1C & D). After weaning, daily energy intake normalized for body weight was higher in ZSD mice, and thus could not account for growth retardation (Fig. 1E).

The presence of an enlarged liver was striking during ZSD mice dissection (Fig. 1F), but no hydronephrosis was detected in contrast to the *Pex1*-G844D C57BL/6N strain reported by Berendse et al. [21]. ZSD mice exhibited progressive relative hepatomegaly as depicted by the increase in liver weight normalized for body weight (Fig. 1G). In addition, absolute ZSD liver weight exceeded controls between 2 and 3 months of age (Supplementary Fig. 1). Berendse et al. suggested that fat accumulation explains this hepatomegaly [21]. We performed both biochemical and histological liver lipid quantification and we could not confirm liver fat accumulation in ZSD mice (Fig. 1H–L). Beside lipids accumulation, sugar and proteins accumulation were ruled out by glycogen metabolism analysis (see below) and protein quantification (Supplementary Fig. 2), respectively.

PBD increases BA and VLCFA levels leading to farnesoid X receptor and PPARα activation which upregulate proliferation markers *Foxm1* and *c-myc*, respectively [21,33,42]. Here we found that *Foxm1*, *c-myc*, *Pcna* and *Mki67* proliferation markers and PPARα target genes were upregulated in ZSD mouse liver (Table 1). To confirm these data, we quantified hepatocytes (HNF4α positive nuclei) and proliferation marker (Ki67 positive nuclei) on liver slides. Proliferative hepatocyte proportion was not different in ZSD livers compared to controls (Fig. 1M, Supplementary Fig. 3). Unexpectedly, this method discovered a higher hepatocyte density that decreased over time in ZSD mice liver (Fig. 1N). ZSD hepatocyte proportion (relative to all liver cells) remained constant during the whole study (Fig. 1O). To further decipher hepatocyte density modification, we measured hepatocyte area and confirmed a progressive ZSD hepatocyte hypertrophy with age (Fig. 1P–R). Based on these findings, we postulate that the progressive hepatomegaly presented by ZSD mice after 1 month of age is explained by hepatocyte hypertrophy and not hepatocyte proliferation.

3.3. Pathological liver analysis revealed reduced peroxisome number, bile duct proliferation and discrete collagen deposition in ZSD mice

The liver of ZSD mice exhibited a strongly reduced PMP70-positive particle number, confirming PBD in this tissue (Fig. 2A). When looking at the H&E-stained liver slides we found that the cytoplasm of control mice hepatocytes presented torn white spaces that were not present in ZSD mice hepatocytes, especially at young age (Fig. 2B). The absence of these spaces suggested an impairment in liver glycogen metabolism in ZSD mice liver (see below). Moreover, in ZSD mice liver, H&E staining highlighted bile duct proliferation and progressive hepatocytes enlargement with age, especially in the centrilobular zone supporting the progressive hepatocyte hypertrophy detected earlier (Fig. 2B). Bile plugs and hepatocellular bile pigments accumulation were detected in 6-month-old ZSD mice liver (Fig. 2B). In line with bile duct proliferation, RNA-seq analysis showed cholangiocytes markers enrichment among the ZSD upregulated genes (Fig. 2C). SR-stained area, a marker of collagen deposition, was slightly but significantly increased in ZSD mice liver along the longitudinal study (Fig. 2D & E). Collagen genes

Table 1
RNA sequencing analysis on 2-month-old control and ZSD mice liver.

Pathway	Symbol	Description	log_2 (fold change)	Fold change	*p*-Value	FDR
Proliferation	Foxm1	Forkhead box M1	1.17	2.25	*	0.0434
	Mki67	Antigen identified by monoclonal antibody Ki 67	1.78	3.43	*	0.0323
	Myc	Myelocytomatosis oncogene	2.07	4.20	***	0.000845
	Pcna	Proliferating cell nuclear antigen	0.34	1.27	*	0.0408
Hypertrophy	Akt1	Thymoma viral proto-oncogene 1	0.23	1.17	*	0.0475
	Mtor	Mechanistic target of rapamycin kinase	0.60	1.51	**	0.00252
	Mrps6	Mitochondrial ribosomal protein S6	0.61	1.53	**	0.000907
	Eif4ebp1	Eukaryotic translation initiation factor 4E binding protein 1	0.36	1.29	*	0.0351
PPARα targets	Acot1	Acyl-CoA thioesterase 1	3.14	8.82	***	0.00000833
	Cd36	CD36 molecule = fatty acid translocase	4.35	20.39	***	7.22E-07
	Cpt1a	Carnitine palmitoyltransferase 1a, liver	0.66	1.58	***	0.000496
	Cpt1b	Carnitine palmitoyltransferase 1b, muscle	2.41	5.31	***	0.00000316
	Cyp4a10	Cytochrome P450, family 4, subfamily a, polypeptide 10	4.59	24.08	***	0.000313
	Myc	Myelocytomatosis oncogene	2.07	4.20	***	0.000845
Synthesis	Afp	Alpha fetoprotein	6.23	75.06	***	7.93E-10
	Alb	Albumin	−0.82	0.57	***	0.00206
	Hmgcr	3-Hydroxy-3-methylglutaryl-Coenzyme A reductase	1.91	3.76	***	0.00289
Collagen deposition	Col1a1	Collagen, type I, alpha 1	0.71	1.63	**	0.0124
	Col1a2	Collagen, type I, alpha 2	0.22	1.17	n.s.	> 0,05
	Col3a1	Collagen, type III, alpha 1	0.77	1.70	***	0.000748
	Col4a2	Collagen, type IV, alpha 2	1.47	2.77	***	1.98E-07
	Acta2	Actin, alpha 2, smooth muscle, aorta	−0.27	0.83	n.s.	> 0,05
Glycogen metabolism	Slc2a2	Solute carrier family 2 (facilitated glucose transporter), member 2 = Glut2	−0.81	0.57	***	0.0000282
	Hk3	Hexokinase 3	−0.80	0.58	**	0.0178
	Gck	Glucokinase	−0.85	0.55	*	> 0,05
	Pgm1	Phosphoglucomutase 1	0.37	1.29	***	0.000349
	Ugp2	UDP-glucose pyrophosphorylase 2	0.04	1.03	n.s.	> 0,05
	Gyg	Glycogenin	1.73	3.32	***	2.01E-07
	Gys2	Glycogen synthase 2	−1.01	0.50	***	0.00177
	Gsk3a	Glycogen synthase kinase 3 alpha	0.24	1.18	**	0.004
	Gbe1	Glucan (1,4-alpha-), branching enzyme 1	−0.27	0.83	**	0.0116
	Agl	Amylo-1,6-glucosidase, 4-alpha-glucanotransferase	−0.40	0.76	***	0.000115
	Pygl	Liver glycogen phosphorylase	−1.00	0.50	***	0.00000337
	G6pc	Glucose-6-phosphatase, catalytic	−2.46	0.18	***	3.98E-07
	Slc37a4	Solute carrier family 37 (glucose-6-phosphate transporter), member 4 = G6pt	−1.21	0.43	***	0.00011
Glycolysis	Slc2a2	Solute carrier family 2 (facilitated glucose transporter), member 2 = Glut2	−0.81	0.57	***	0.0000282
	Hk3	Hexokinase 3	−0.80	0.58	**	0.0178
	Gck	Glucokinase	−0.85	0.55	*	> 0,05
	Gpi1	Glucose phosphate isomerase 1	0.51	1.42	***	0.00002
	Pfkl	Phosphofructokinase, liver, B-type	0.24	1.18	n.s.	> 0,05
	Pfkfb1	6-Phosphofructo-2-kinase/fructose-2,6-biphosphatase 1	−0.86	0.55	***	0.0022
	Aldob	Aldolase B, fructose-bisphosphate	−0.09	0.94	n.s.	> 0,05
	Tpi1	Triosephosphate isomerase 1	−0.27	0.83	**	0.00518
	Gapdh	Glyceraldehyde-3-phosphate dehydrogenase	−0.07	0.95	n.s.	> 0,05
	Pgk1	Phosphoglycerate kinase 1	0.22	1.17	**	0.0089
	Pgam1	Phosphoglycerate mutase 1	0.06	1.05	n.s.	> 0,05
	Eno1	Enolase 1, alpha non-neuron	−0.19	0.88	n.s.	> 0,05
	Pklr	Pyruvate kinase liver and red blood cell	−1.02	0.49	***	0.00269
Gluconeogenesis	Pck1	Phosphoenolpyruvate carboxykinase 1, cytosolic	−1.19	0.44	**	0.00179
	Eno1	Enolase 1, alpha non-neuron	−0.19	0.88	n.s.	> 0,05
	Pgam1	Phosphoglycerate mutase 1	0.06	1.05	n.s.	> 0,05
	Pgk1	Phosphoglycerate kinase 1	0.22	1.17	**	0.0089
	Gapdh	Glyceraldehyde-3-phosphate dehydrogenase	−0.07	0.95	n.s.	> 0,05
	Tpi1	Triosephosphate isomerase 1	−0.27	0.83	**	0.00518
	Aldob	Aldolase B, fructose-bisphosphate	−0.09	0.94	n.s.	> 0,05
	Pfkfb1	6-Phosphofructo-2-kinase/fructose-2,6-biphosphatase 1	−0.86	0.55	***	0.0022
	Fbp1	Fructose bisphosphatase 1	−0.08	0.94	n.s.	> 0,05
	Gpi1	Glucose phosphate isomerase 1	0.51	1.42	***	0.00002
	G6pc	Glucose-6-phosphatase, catalytic	−2.46	0.18	***	3.98E-07
	Slc37a4	Solute carrier family 37 (glucose-6-phosphate transporter), member 4 = G6pt	−1.21	0.43	***	0.00011
	Slc2a2	Solute carrier family 2 (facilitated glucose transporter), member 2 = Glut2	−0.81	0.57	***	0.0000282

Modulation of genes related to hepatocytes proliferation and hypertrophy, to targets of PPARα, to liver collagen deposition and biochemically relevant in glycogen and glucose metabolism (ZSD *versus* control mice liver, n = 6/group).
FDR: false discovery rate, PPARα: peroxisome proliferator-activated receptor alpha.
*** *p*-Value < 0,001.
** *p*-Value < 0,01.
* *p*-Value < 0,05.

(*Col1a1*, *Col1a2*, *Col3a1* and *Col4a2*) were significantly upregulated (1.2 to 2.8-fold) in ZSD mice liver (Table 1) in line with increased SR staining. Together, histopathological studies of the liver highlighted clues to liver glycogen metabolism alteration (see below), mild collagen deposition, cholestasis and bile duct proliferation supported by RNA-seq analysis.

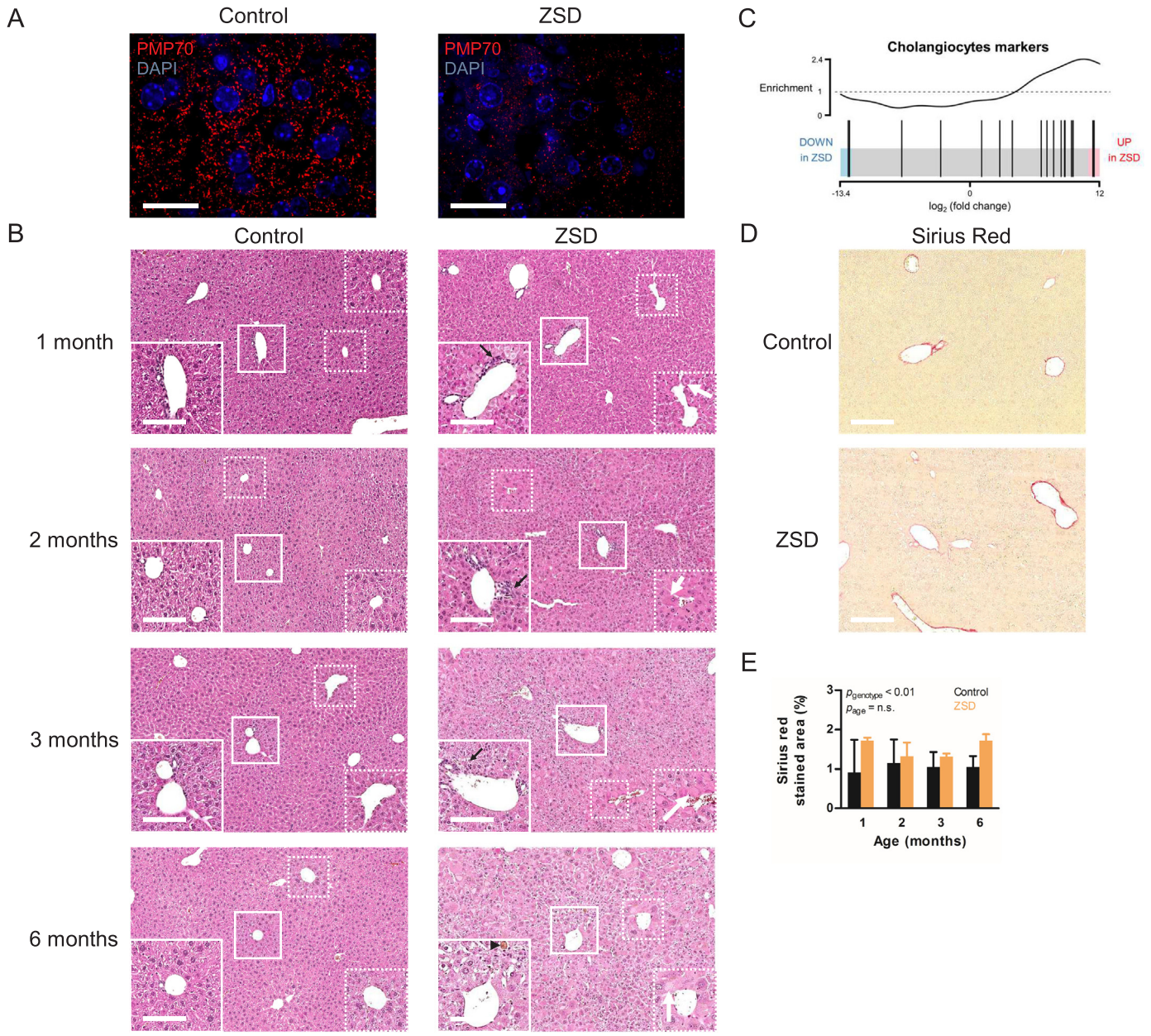

Fig. 2. Zellweger spectrum disorder (ZSD) mouse liver contained less peroxisomes, showed bile duct proliferation and discrete collagen deposition. (A) 2-month-old mouse liver immunolabelled for 70-kDa peroxisomal membrane protein (PMP70) and nuclei stained with diamidino-2-phenylindole dihydrochloride (DAPI). ZSD mouse hepatocytes contained less peroxisomes than control. Representative pictures of 2 livers/genotype. Scale bar: 20 μm. (B) Longitudinal study of H&E stained liver slides. Inserts show higher magnification of the periportal space (boxed area) or centrilobular zone (dashed boxed area). ZSD portal spaces showed bile duct proliferation (black arrow). ZSD mice hepatocytes enlarged progressively and contained pale eosinophilic material (white arrow) especially in the centrilobular zone. Bile plugs were seen in 6-month-old ZSD mouse liver (arrowhead). Representative pictures of 6 livers/timepoint/genotype. Scale bar: 200 μm. (C) Barcode plot illustrating cholangiocyte markers expression enrichment in 2-month-old mouse liver (n = 6/genotype). Comparison of ZSD *versus* control detected enrichment of cholangiocyte markers in ZSD mice liver upregulated genes in line with the bile duct proliferation seen on ZSD mice liver H&E slides. (D) 6-month-old mice liver stained with Sirius red (SR) exhibited a slight increase in perivascular collagen deposition in ZSD samples. Representative pictures of 6 livers/genotype. Scale bar: 200 μm. (E) Longitudinal morphometry study of SR-stained liver slides unveiled a slight but significant increase in SR-stained area in ZSD livers. Two-way ANOVA, n = 6/timepoint/genotype, median ± interquartile range, n.s.: not significant.

3.4. ZSD mice exhibited severe liver glycogen metabolism impairment leading to poor fasting resistance

Liver glycogen metabolism alterations were reported previously in a liver-restricted PBD mouse model and in some ZSD patients [19,43–45]. This, together with the ZSD hepatocytes' aspect, led us to evaluate whether liver glycogen metabolism was altered in our mouse model. PAS stained area was markedly reduced in ZSD mice liver, supporting an altered glycogen content (Fig. 3A–B). The difference tended to disappear with age as detected by both PAS staining and biochemical glycogen quantification (Fig. 3B & C). PAS stained area correlated significantly with glycogen content in ZSD mice liver (Fig. 3D). Furthermore, PAS staining was amylase-sensitive supporting the presence of glycogen (Fig. 3F & G). Our ZSD mice exhibited slightly decreased fed-glycemia and poor fasting resistance (Fig. 3E & K, Supplementary Fig. 4). Both were not related to daily energy intake (Fig. 1E). RNA-seq revealed glycogen metabolism genes enrichment in the downregulated ZSD liver genes (Fig. 3J). Among those genes, *G6pc* was downregulated

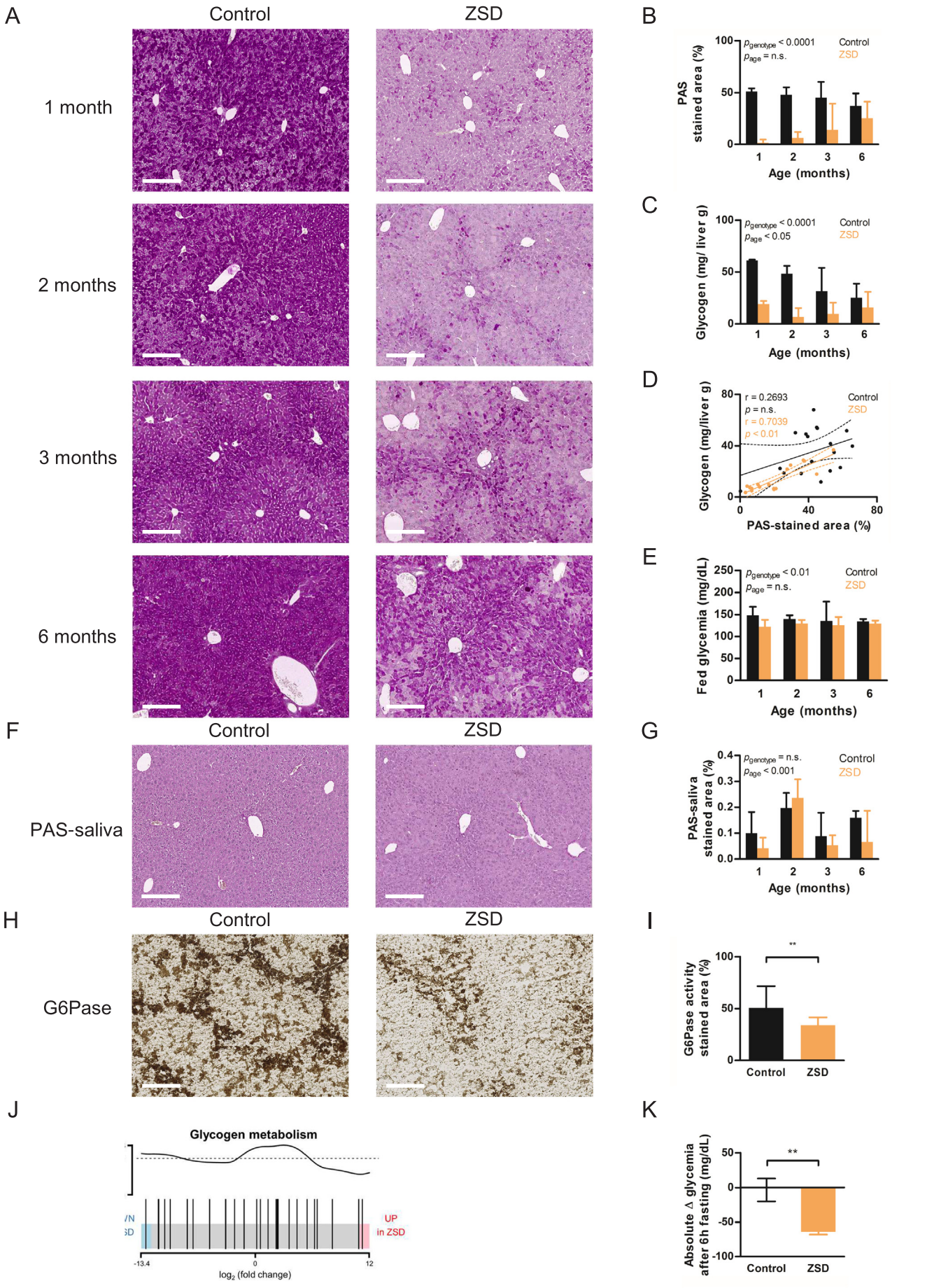

(caption on next page)

Fig. 3. Zellweger spectrum disorder (ZSD) mouse liver exhibited glycogen metabolism alterations leading to poor fasting resistance. (A) Longitudinal study of Periodic-acid Schiff (PAS) stained liver slides unveiled a severe lack of staining in ZSD mouse liver compared to control. The difference tended to decrease with age. (B) Longitudinal morphometry study of PAS stained liver slides confirmed the lower PAS-stained area in ZSD. PAS staining in control mouse liver tended to decrease with age, opposite to what was detected in ZSD mice liver ($p_{interaction} < 0.01$). (C) Biochemical liver glycogen content quantification normalized for liver weight confirmed a decreased glycogen content in ZSD. An inverted trend with age was detected in controls compared to ZSD samples ($p_{interaction} = 0.016$). (D) Scatterplot showing the correlation between PAS-stained area and glycogen content in mouse liver. Both measures were tightly correlated in ZSD mice liver. (E) Mouse morning glycemia was lower in ZSD, especially in 1-month-old mice. (F) 2-month-old control and ZSD liver slides stained with PAS after saliva exposure lead to nearly complete PAS staining disappearance. It meant that PAS-stained area was amylase-sensitive sugar (*i.e.* glycogen). (G) Longitudinal morphometry study of mouse liver slides stained with PAS after saliva exposure detected no statistical difference between both genotypes. (H) 2-month-old control and ZSD liver unfixed slides stained for glucose-6-phosphatase activity (G6Pase) unveiled classical periportal space zonation with a dramatic activity decrease in ZSD liver. (I) G6Pase activity stained area quantification confirmed the difference between ZSD liver and control group. (J) Barcode plot illustrating glycogen metabolism genes expression enrichment in 2-month-old mouse liver ($n = 6$). Comparison of ZSD *versus* control unraveled enrichment of glycogen metabolism genes in ZSD mouse liver downregulated genes in line with the lower ZSD mouse liver glycogen content. (K) Absolute glycemia variation after 6 h fasting of 2-month-old mice lead to severe glycemia drop in ZSD mice compared to no variation in control. This confirmed the physiological impact of lower glycogen content in ZSD mice liver. Representative pictures of 6 livers/timepoint/genotype. Scale bar: 200 μm. Two-way ANOVA and n = 6/timepoint/genotype (longitudinal), Spearman's correlation test and $n = 18$/genotype (correlation) or Mann-Whitney test and n = 6/genotype (2 groups), median ± interquartile range (bars) or best-fit line ± 95% confidence band (scatter-plot), n.s.: not significant, r: correlation coefficient, **: p-value < 0.01.

by 5.5-fold in ZSD mouse live (Table 1). *G6pc* encodes G6Pase which is responsible for the last step in liver glucose release pathway. To ascertain *G6pc* downregulation impact, we analyzed G6Pase activity on liver tissue and found that the G6Pase activity-stained area was significantly reduced in ZSD mice liver (Fig. 3H & I). Thus, our ZSD mouse model exhibited liver glycogen metabolism alteration with clinical consequence (*i.e.* poor fasting resistance) which could be used as a robust readout in preclinical studies.

3.5. ZSD mice liver expression profile unraveled modulations in multiple pathways among which glucose metabolism was switched to glucose consumption

The principal component analysis performed on estimated transcript abundances derived from RNA-seq data unmasked 3 different gene expression profiles (control males, control females and ZSD mice) suggesting that gender impacted more strongly the gene expression in control than in ZSD liver (Fig. 4A). Large numbers of genes (7102 and 5028) were significantly modulated (using FDR cut-off of 0.05 and 0.01, respectively) between control and ZSD mice liver (Fig. 4B). Over-representation analysis of gene ontology analysis exposed modulations in multiple molecular functions, biological process and cellular components associated with PBD (Fig. 4C, Supplementary Figs. 5 & 6).

The liver glycogen alterations discovered in our ZSD mouse model and the link between carbohydrate metabolism and peroxisome biogenesis, led us to evaluate glucose metabolism gene expression modulation by enrichment analysis [19,45]. In ZSD liver, glycolysis genes were enriched in the upregulated genes and opposed to gluconeogenesis gene enrichment in the downregulated genes (Fig. 4D). A comparison between the modulation levels from Peeters et al. gene list and our RNA-seq data uncovered a significant correlation suggesting similar PBD impact on liver gene expression in both mouse models (Fig. 4E and Supplementary Table 2). Liver RNA-seq analysis provided insight into the entire breadth of PBD consequences.

3.6. ZSD MEF biochemical and immuno-labelling analysis highlighted PBD

MEF were collected to study *in vitro* peroxisome functionality. MEF VLCFA content was elevated in ZSD donor compared to control, specifically C_{26} and C_{26}/C_{22} and C_{24}/C_{22} ratios were significantly increased (Fig. 5A–E). Phytanic and pristanic acids were not detected because they are absent from cell medium and they are not synthetized by MEF (data not shown). Peroxisome biogenesis was evaluated by immunofluorescent staining for catalase (peroxisomal matrix enzyme) and PMP70 (peroxisomal membrane protein) which highlighted a decreased catalase import into peroxisomes in ZSD MEF compared to control (Fig. 5F). Some ZSD MEF exhibited catalase import competent peroxisomes beside cells devoid of this competence. This phenomenon called peroxisomal mosaicism is classically described in cells from milder ZSD patients [2]. eGFP-PTS1, a fluorescent peroxisomal reporter, was expressed in MEF and lead to a more diffuse signal with lighter peroxisome staining in ZSD donor than in control (Fig. 5F). Together, these data suggest that ZSD MEF is a robust mild ZSD cell model for *in vitro* studies before going for *in vivo* evaluation.

3.7. ZSD mice presented multiple biochemical alterations resulting from PBD

To characterize the biochemical alterations present in our novel ZSD mice strain, we assessed the main biochemical markers found altered in ZSD patients.

3.7.1. Odd-numbered dicarboxylic aciduria was detected in ZSD mice

We collected urine samples from 2-month-old mice to evaluate their organic acids profile. Globally, ZSD mice urine samples contained higher amount of ketone bodies (3-OH butyric acid), dicarboxylic acids (adipic, pimelic, suberic, azelaic and sebacic acids), 2- and 3-hydoxysebacic acid, Krebs' cycle intermediates (fumaric and succinic acids), glycolic acid and 2-OH-glutaric acid (Fig. 6A). The odd-numbered dicarboxylic aciduria (pimelic and azelaic aciduria) is thought to arise from microsomal α-hydroxylation of the accumulated VLCFA, followed by their oxidative decarboxylation to odd-chain VLCFA and ended by microsomal ω-oxidation of these intermediates to produce odd-numbered dicarboxylic acids that accumulate owing to peroxisomal ß-oxydation impairement [8,9]. These urinary data correlate with findings in ZSD patients and reflect PBD consequence on multiple organs [8]. This feature is important as it might serve as global readout for ZSD pre-clinical studies.

3.7.2. Plasma liver markers levels depicted chronic liver injury in ZSD mice

Liver disease is present in nearly all ZSD patients. Therefore, we evaluated several hepatic markers in our mouse model [3]. Plasma from ZSD mice showed signs of hepatocyte injury as highlighted by GPT elevation and albumin decrease (Fig. 6B). In ZSD mice liver, albumin (*Alb*) expression was reduced by nearly 50% and the liver injury/tumor marker *Afp* was upregulated more than 50-fold in line with the suspected hepatocellular insult (Table 1). Total bilirubin and alkaline phosphatases activity and, to a lesser extent, gGT elevation suggested cholestasis in ZSD mouse plasma. As for ZSD patients, we found that these markers tended to normalize with age (Fig. 6B) [4].

3.7.3. Erythrocyte plasmalogen, plasma pipecolic acid and C26LPC levels were consistent with PBD in ZSD mice

Plasmalogen biosynthesis starts inside peroxisomes and their erythrocytes level is used as diagnostic marker for several peroxisomal disorders [46]. $C_{16:0}$ erythrocyte plasmalogen levels were reduced in

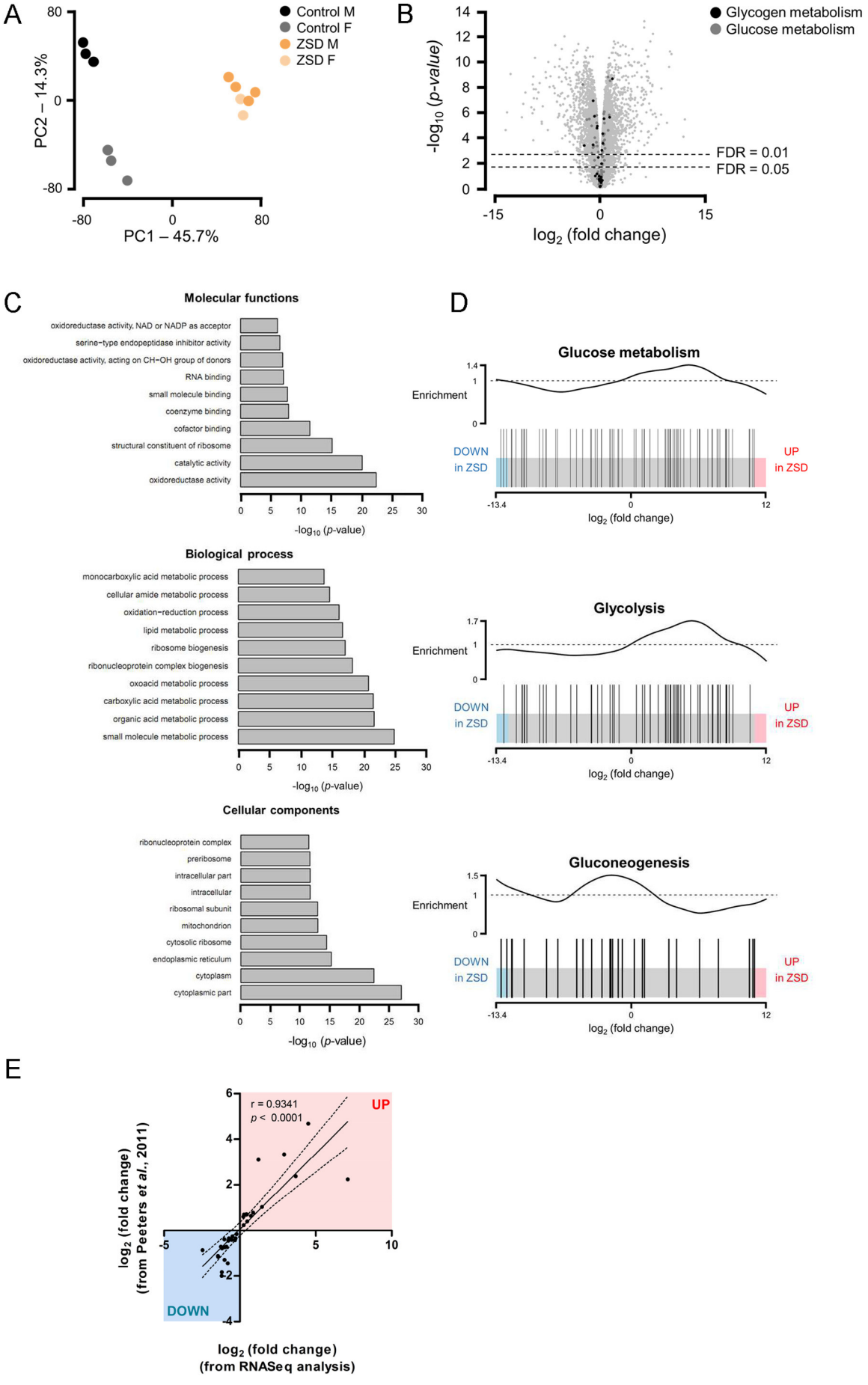

(caption on next page)

Fig. 4. Zellweger spectrum disorder (ZSD) mouse liver gene expression profile unveiled modulations in multiple pathways among which glucose metabolism was switched to glucose consumption. (A) Scatterplot of the principal component analysis performed on estimated transcript abundances derived from RNA sequencing data collected from 2-month-old control and ZSD mice liver (n = 6/genotype) showed 3 clouds from control males, control females and ZSD mice samples, respectively. This could mean that liver sex phenotype was lost as peroxisome biogenesis disorder consequence. PC1 and PC2 explained 45.7% and 14.3% of the variability, respectively. (B) Volcano plot from RNA sequencing analysis represented > 7000 or 5000 significantly (false discovery rate (FDR) < 0.05 or < 0.01, respectively) modulated genes (ZSD *versus* control). Glycogen (black) and glucose (grey) metabolism genes were plotted to highlight their position on the whole analysis. (C) Gene ontology enrichment analysis for molecular functions, biological process and cellular components highlighted significant enrichment in multiple pathways reflecting the vast peroxisome biogenesis disorder consequences on liver gene expression. (D) Barcode plot illustrating glucose metabolism genes expression enrichment in ZSD *versus* control mice liver (n = 6/genotype), no modulation trend was detected. Analysis was further refined to analyze glycolysis and gluconeogenesis independently. This unraveled glycolysis genes enrichment among upregulated genes, in association with gluconeogenesis genes enrichment among downregulated genes. Expression profile in ZSD mouse liver suggested a glucose metabolism switch to glucose consumption. (E) Scatter plot showing significant correlation between gene expression modulation (ZSD *versus* control liver) in our study and reported by Peeters et al. in 2011. Spearman's correlation test, r: correlation coefficient, best-fit line ± 95% confidence band.

ZSD mice older than 1 month (Fig. 6C). Some patients with mild ZSD phenotype may exhibit normal erythrocyte plasmalogens levels as were $C_{18:0}$ erythrocyte plasmalogens in ZSD mice older than 1 months [3]. Pipecolic acid, a metabolite resulting from lysine degradation, accumulated in ZSD mice plasma highlighting a defect during its hepatic peroxisomal degradation (Fig. 6D). Quantification of C26LPC is used for the newborn screening of X-linked adrenoleukodystrophy, another peroxisomal disorder, and it was shown that C26LPC is also an effective ZSD marker [47,48]. In ZSD mice, C26LPC levels were increased and thus confirmed the ZSD phenotype of our mouse model (Fig. 6E).

For pre-clinical purposes, erythrocyte plasmalogen and plasma pipecolic acid levels could be used as proxy for bone marrow and liver PBD status, respectively [46,49].

3.7.4. BCFA and VLCFA accumulated in ZSD mice plasma and liver

Peroxisomes are responsible for BCFA (phytanic and pristanic acids) and VLCFA metabolism driving us to study them in our mouse model [6]. ZSD mice exhibited BCFA and VLCFA accumulation in both plasma and liver (Fig. 7 A-G). Plasma and liver phytanic acid and C_{26} levels showed a significant decrease with age in ZSD mice along with significant correlation between plasma and liver levels (Fig. 7A & F). These correlations suggest that plasma BCFA and VLCFA levels quantification could be used as a proxy for intra-hepatic levels during treatment evaluation in ZSD mice.

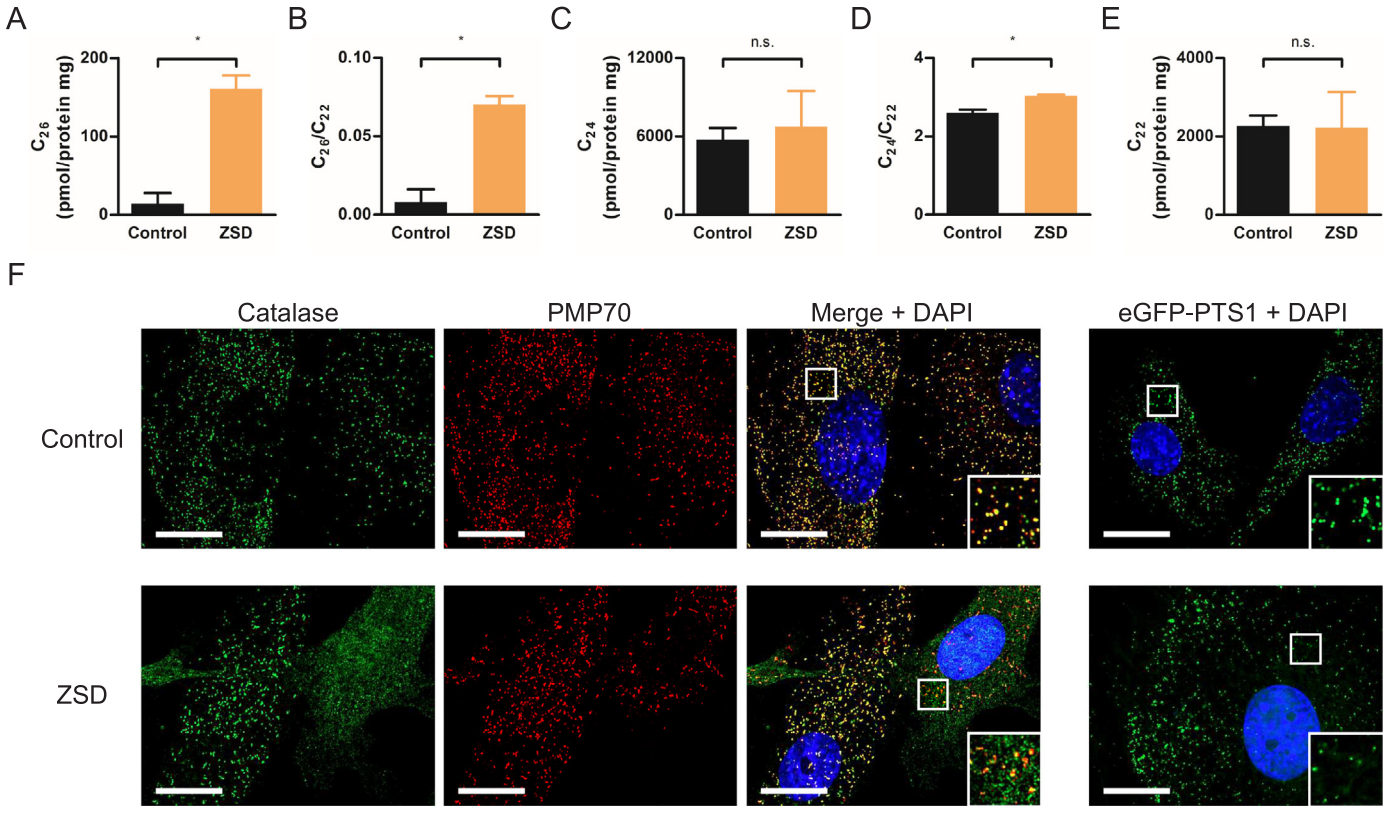

Fig. 5. Zellweger spectrum disorder (ZSD) mouse embryonic fibroblasts (MEF) biochemical evaluation and peroxisome staining highlighted peroxisome biogenesis disorder (PBD) stigma. Very long chain fatty acids (A) C_{26}, (C) C_{24} and (E) C_{22} were quantified in control and ZSD MEF and normalized for protein content. C_{22} was used to calculate (B) C_{26}/C_{22} and (D) C_{24}/C_{22} ratios, both were elevated in ZSD cells. ZSD cells accumulated C_{26} and C_{24} as a consequence of the PBD caused by *Pex1*-G844D homozygous mutation. Mann-Whitney test, n = 4, median ± interquartile range, *: p-value < 0.05, n.s.: not significant. (F) Control and ZSD MEF were stained for a peroxisomal matrix protein (catalase), and 70-kDa peroxisomal membrane protein (PMP70) to evaluate peroxisome biogenesis reflected by both markers colocalization. In a second time, MEF were transduced to express green fluorescent protein linked to peroxisome targeting signal 1 (eGFP-PTS1). Nuclei were stained with diamidino-2-phenylindole dihydrochloride (DAPI). Inserts show higher magnification of the boxed area. ZSD MEF harbored PMP70-positive granules without corresponding catalase staining (peroxisome ghosts) confirming PBD. Some ZSD cells contained catalase import competent peroxisomes, a phenomenon known as peroxisomal mosaicism. ZSD MEF exhibited a more diffuse eGFP-PTS1 signal in the cytoplasm than control cells, highlighting PBD. Scale bar: 20 μm.

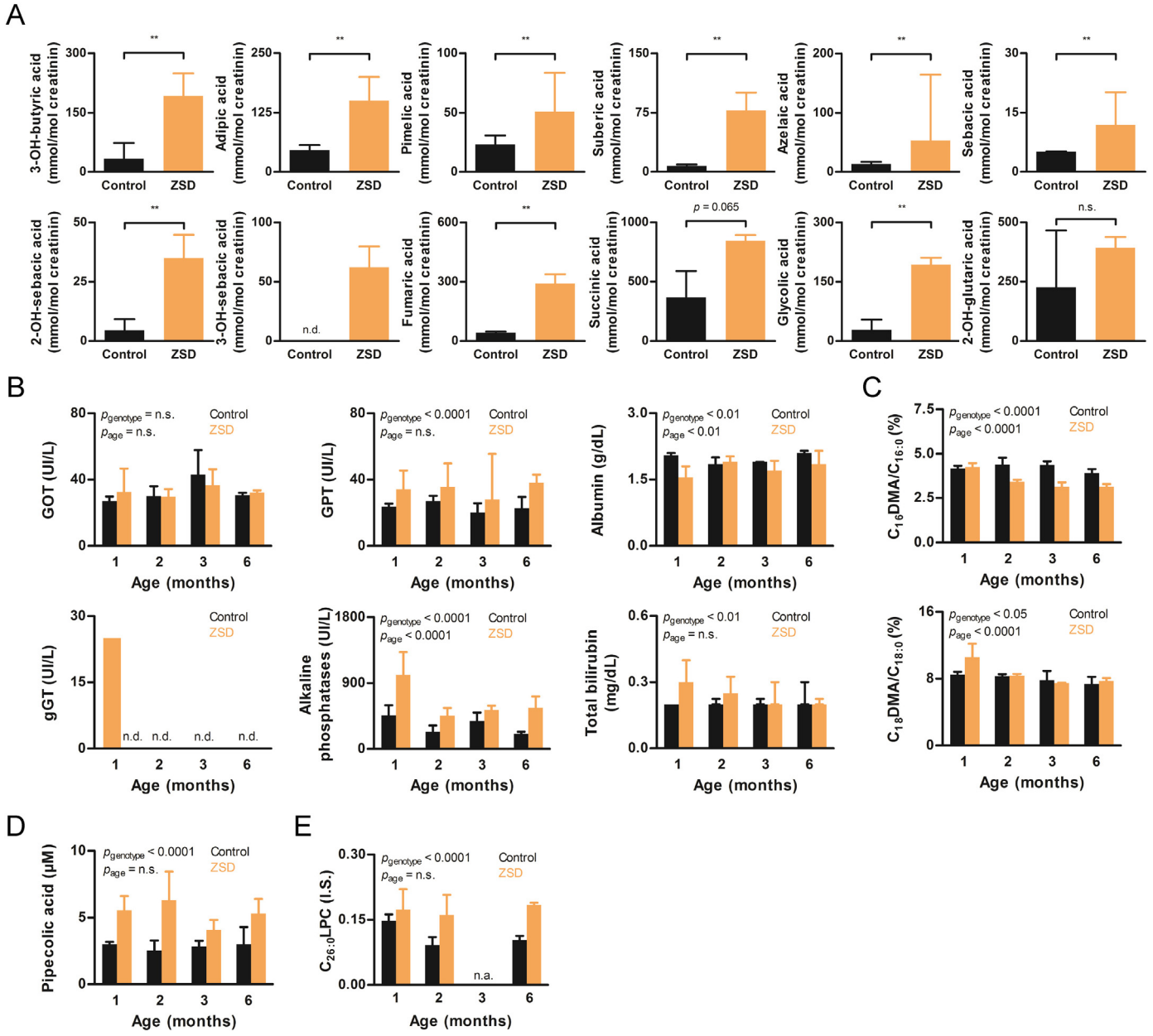

Fig. 6. Zellweger spectrum disorder (ZSD) mice urine organic acid profile, blood peroxisome markers and plasma liver markers fitted with a ZSD. (A) Relevant organic acids detected in 2-month-old mouse urine. In ZSD mouse samples, a broad dicarboxylic aciduria was present from C_6 (adipic acid) to C_{10} (sebacic acid) including odd-numbered acids. As reported for ZSD patients, hydroxylated sebacic acid derivatives and Krebs cycle intermediates (succinic and fumaric acids) were significantly increased in ZSD mice urine. (B) Longitudinal study of plasma liver enzymes and cholestasis markers suggested a chronic liver injury (low albumin level at 1 month and persistent glutamate-pyruvate transaminase (GPT) elevation) associated to progressive improvement of the cholestasis (alkaline phosphatase level decrease and total bilirubin normalization) in ZSD mice. (C) Erythrocyte plasmalogen content was studied longitudinally and was reported as the ratio between $C_{16:0}$ or $C_{18:0}$ dimethyl acetal (DMA) and the corresponding fatty acid. Plasmalogens are partly synthetized by peroxisomal enzymes thus explaining lower $C_{16:0}$ erythrocytes plasmalogen levels in ZSD mice older than 1 month. Yet, erythrocytes plasmalogen levels can be normal in mild ZSD patients as were $C_{18:0}$ erythrocytes plasmalogen levels in ZSD mice. (D) Plasma pipecolic acid (PA) levels were significantly elevated in ZSD mice as a result of its impaired degradation by the peroxisome. (E) $C_{26:0}$lysophosphatidylcholine (C26LPC) quantified on dried blood spot revealed increased levels in ZSD mice. C26LPC marker is used for newborn screening of X-linked adrenoleukodystrophy, a related peroxisomal disorder, and it is proposed as a sensitive marker for ZSD diagnosis. Data are expressed as a ratio between the signal of the analyte and the signal of its internal standard (I.S.). Mann-Whitney test and $n = 6$/genotype (2 groups) or two-way ANOVA, n = 6/timepoint/genotype (longitudinal), median ± interquartile range, n.d.: not detected, n.s.: not significant, GOT: glutamate-oxaloacetate transaminase, gGT: gamma-glutamyltransferase, n.a.: not available, **: p-value < 0.01.

3.7.5. ZSD mice were cholestatic and accumulated oxysterols and C_{27}-BA precursors in plasma and liver

PBD are known to induce altered BA metabolism [50]. Therefore, we decided to analyze C_{24} BA and their C_{27} precursors (di- and trihydroxycholestanoic acids) in ZSD mice plasma and liver. Total (un)conjugated C_{24} BA levels were not significantly different in ZSD and control mice plasma (Fig. 8A & B). Yet, total (un)conjugated C_{24} BA levels were significantly reduced in ZSD mice liver, the organ in which they are produced. The total (un)conjugated C_{24} BA plasma-liver ratio was higher in ZSD mice, highlighting the discrepancy between total (un)conjugated C_{24} BA plasma and liver levels in ZSD mice, compared to control. Moreover, a significant positive correlation was detected

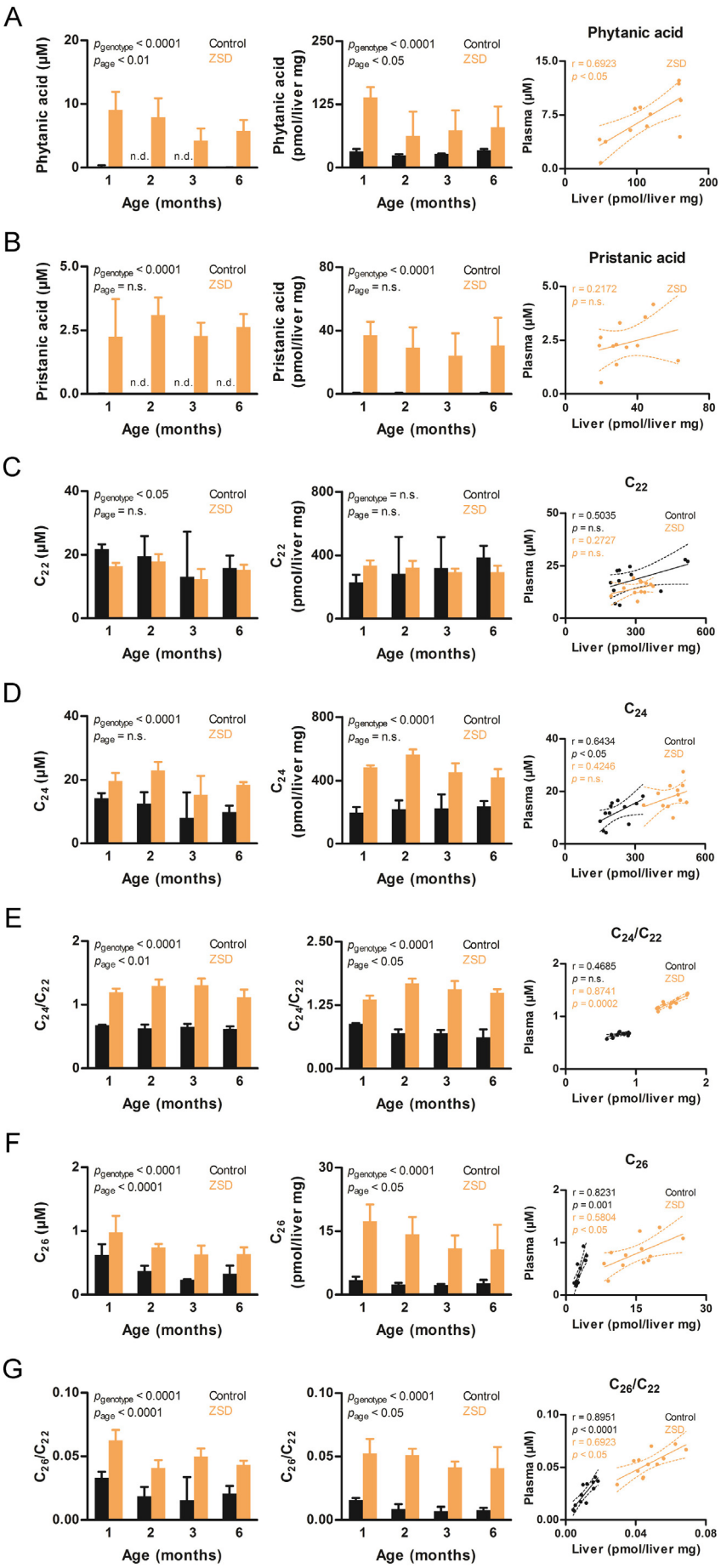

Fig. 7. Zellweger spectrum disorder (ZSD) mouse plasma and liver displayed branched-chain and very long-chain fatty acid accumulation. Phytanic acid and C26 levels were correlated between the two compartments and tended to normalize with age. Longitudinal study of control (black) and ZSD (orange) mouse (A) phytanic and (B) pristanic acids and (C) C_{22}, (D) C_{24}, (E) C_{24}/C_{22}, (F) C_{26}, (G) C_{26}/C_{22} levels in plasma and liver and their correlation on scatter plot. Two-way ANOVA and n = 6/timepoint/genotype reported as median ± interquartile range (longitudinal), Spearman's correlation test and n = 12/genotype with best-fit line ± 95% confidence band (correlation), r: correlation coefficient, n.s.: not significant.

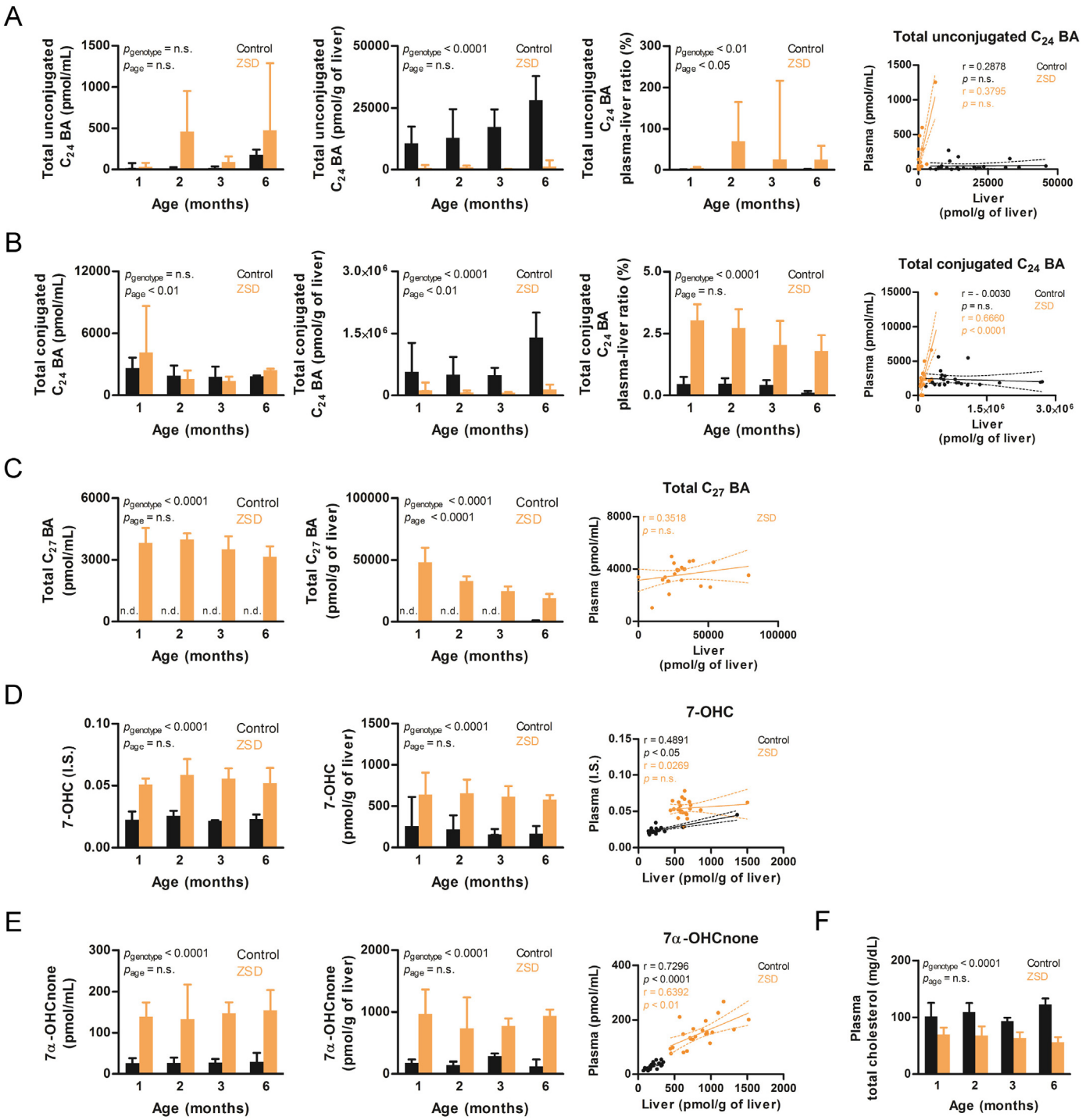

Fig. 8. Zellweger spectrum disorder (ZSD) mouse plasma and liver total C24 bile acids (BA) levels underlined cholestasis associated with specific oxysterol species and C27 BA accumulation and decreased plasma total cholesterol levels. Longitudinal study of control (black) and ZSD (orange) mouse (A) total unconjugated C_{24} BA, (B) total conjugated C_{24} BA, (C) total C_{27} BA, (D) 7-hydroxycholesterol (7-OHC), (E) 7α-hydroxycholestenone (7α-OHCnone), (F) total cholesterol in plasma and liver and their correlation on scatter plot (excepted for total cholesterol). Un- and conjugated C_{24} BA plasma to liver ratios highlighted cholestasis (*i.e.* plasma BA accumulation) in ZSD mice. C_{27} BA precursors were only detected in ZSD mice thus confirming the relative interruption between C_{27} and C_{24} BA, just as in human PBD. Both 7-OHC and 7α-OHCnone are formed during initial BA biosynthesis steps and accumulated in ZSD mouse samples. Plasma total cholesterol levels were lower in ZSD mice. Two-way ANOVA and n = 5–6/timepoint/genotype reported as median ± interquartile range (longitudinal), Spearman's correlation test and n = 21/genotype with best-fit line ± 95% confidence band (correlation), r: correlation coefficient, n.s.: not significant.

between conjugated C_{24} BA plasma and liver levels in ZSD mice, but not in control. Finally, C_{27} BA precursors were only detected in ZSD mice plasma and liver (Fig. 8C), which confirms that our model induces a relative interruption between C_{27} and C_{24} BA, just as in human PBD. Taken together, these results unraveled a total C_{24} BA accumulation in ZSD mice plasma along with a defect in their plasmatic elimination.

This cholestasis, a well-known phenomenon in ZSD patients, supports our finding of increased plasma cholestasis markers (Fig. 6B) [11]. From these results, we wanted to go further and investigate the consequences of this C_{27} and C_{24} BA accumulation at the oxysterol level,

the early metabolites of cholesterol. We found that both 7-hydroxycholesterol (7-OHC) and 7α-hydroxy-4-cholesten-3-one (7α-OHC-none), formed during initial steps of BA synthesis, were elevated in ZSD mice liver and plasma and showed no evolution with age (Fig. 8D & E). We also analyzed total cholesterol and found that its levels were decreased in ZSD mice plasma (Fig. 8F). These results, together with the 3.8-fold *Hmgcr* upregulation in ZSD mice liver (Table 1), suggest an increased production rate of oxysterols along with a positive-feedback increased biosynthesis of cholesterol.

4. Discussion

To overcome ZSD mouse model limitations (*i.e.* small litters and poor survival rates), the hypomorphic *Pex1*-G844D allele was backcrossed in NMRI background while retaining ZSD mouse phenotype. NMRI ZSD mice exhibited growth retardation, relative hepatomegaly associated to chronic liver injury, hepatocyte hypertrophy and severe liver glycogen metabolism impairment which led to reduced fasting resistance in ZSD mice. Liver RNA-seq underlined the modulation of glycogen metabolism gene expression associated with a switch in glucose metabolism to glucose consumption. We reported multiple peroxisomal biochemical alterations in the ZSD mice, including phytanic acid and C_{26} levels elevation, which tended to normalize with age, along with a specific ZSD urine organic acids profile. Moreover, through correlation between plasma and liver BA levels we could put forth the presence of cholestasis in ZSD mice.

Hepatomegaly is a common finding in ZSD patients, and it was previously described in *Pex1*-G844D C57BL/6N mouse model [3,11,21]. In our mouse model, neither fat accumulation, nor sugar (*i.e.* glycogen) accumulation, nor protein accumulation, nor hepatocyte proliferation could account for the relative hepatomegaly we observed. However, hepatocyte proliferation analysis highlighted an increased hepatocyte density in 1-month-old ZSD mice livers (Fig. 1N). We postulate that hepatocyte proliferation took place before this age to explain the higher hepatocyte density detected in young ZSD mice liver and that the further progressive hepatocyte hypertrophy (Fig. 1P–R) accounted for the relative hepatomegaly developing after this age. The Akt/mTORC1 pathway is a major player in hepatocyte hypertrophy and could be involved in our model (Table 1) [51,52].

Liver injury and fibrosis were less severe in NMRI ZSD mice than in previous *Pex1*-G844D mouse models [21,22]. Background differences could account for this as it was shown for liver fibrosis response to carbon tetrachloride treatment [53,54]. Liver disease was responsible for severe lethality in Berendse et al. mouse model and we postulate that *Pex1*-G844D backcrossing to NMRI background lead to reduced liver response to PBD insult.

Hiebler et al. developed *Pex1*-G844D mouse model in a C57BL/6 × 129 mixed genetic background and bred it with C57BL/6N wild type mice [22]. We bought heterozygous *Pex1*-G844D mice recovered through pure C57BL/6N mouse fertilization with *Pex1*-G844D cryopreserved sperm from Hiebler et al. colony. This process relatively increased the C57BL/6N background and larger homozygous regions could explain the strongly reduced C57BL/6N ZSD mice survival in our experience compared to Hiebler et al.

ZSD mouse background switch was previously successfully evaluated in *Pex2* KO mouse model [55]. Switch from C57BL/6 × 129Sv to Swiss Webster × 129SvEv background increased survival rate but no data about litters yield is available [17]. Survival rate differences between *Pex1*-G844D knockin mouse models and *Pex2* [17,55], *Pex5* [16] and *Pex*13 [18] KO mouse models are explained by the *Pex1*-G844D protein normal stability and residual functionality compared to lack of protein activity in KO models [21,23].

Our ZSD mouse model survival rate was increased by 33% (p-value = 0.07) to 390% (p-value < 0.0001) compared to previous *Pex1*-G844D mouse models [21,22]. Yet, peroxisomal metabolites anomalies displayed by NMRI ZSD mice were similar to previously published *Pex1*-G844D mouse models. For example, compared to control, ZSD mice C_{26} plasma levels were increased by 1.8-fold and 1.6-fold in our study and in Hiebler et al., respectively [22]. Similarly, peroxisomal mosaicism was present in both ZSD MEF from our study and from Berendse et al. [21]. Peroxisomal mosaicism is described in cells from milder ZSD patients [2]. Thus, we postulate that there is no difference in PBD severity that could explain the increased survival rate in our study compared to other *Pex1*-G844D mouse models [21,22].

Pex1-G844D backcrossing in NMRI background exhibit ZSD phenotype similarly to what was published previously regarding (intrauterine) growth retardation [16–18,21,22], relative hepatomegaly [21], plasma and liver peroxisomal metabolites accumulation [21], plasma cholesterol levels and endoplasmic reticulum stress [56–58] and liver glycogen metabolism alterations [19,21] which were also reported in PBD Drosophila model [45]. Liver gene expression modulations were similar to what was reported in a liver-restricted *Pex5* KO mouse model [19].

We went further in deciphering plasma-liver BA and VLCFA correlation to highlight cholestasis and plasma VLCFA level use as a proxy for liver VLCFA content, respectively. Based on our experience with hepatocyte and liver transplantation in ZSD patients, we propose these markers as pre-clinical readout for liver-targeted therapies evaluation in our mouse model [12–14,59]. Plasma VLCFA level would be measured longitudinally during treatment follow-up. Since plasma-liver BA analysis requires mice euthanasia, it would be evaluated only at the end of the protocol.

To our knowledge, this is the first time ZSD mice urine organic acids profiles were analyzed and they were similar to ZSD patients [3,4,8,9]. Moreover, longitudinal peroxisomal metabolites study allowed us to underline a trend to normalization for some markers as it was reported for ZSD patients [4]. These data suggest that our mouse model recapitulate the biochemical history of ZSD patients required for robust pathophysiological studies.

Further studies are needed to evaluate the central nervous system and sensorineural involvement in NMRI ZSD mice. Neither seizures nor severe hypotonia were observed clinically in contrast what was reported for *Pex* KO mouse model [16–18]. Evaluation of the post-transcriptional regulation of modulated genes in ZSD mouse liver would also be of interest (*e.g.*, *Hmgcr*, *Gys2*, …). Furthermore, studying liver glycogen metabolism alterations in ZSD patients liver biopsy would be of great interest because these anomalies were only deeply characterized in ZSD mouse and Drosophila model [19,45]. A recent paper evaluated liver histology in 13 ZSD patients but glycogen metabolism impairment was not discussed [60].

Large litters, high survival rate and ZSD bio-clinical phenotype make this NMRI ZSD mouse model highly suitable for the evaluation of liver-targeted therapies. This is very relevant from a translational point of view given the known liver impact on brain development in ZSD [61] and the encouraging bio-clinical results obtained after liver transplantation in ZSD patients [13,14,59].

5. Conclusion

Pex1-G844D NMRI mouse model is a robust mild ZSD mouse model exhibiting classical clinical, biochemical and liver anomalies associated with PBD. This makes *Pex1*-G844D NMRI mouse model a good candidate for liver cell and gene therapies evaluation in ZSD.

Supplementary data to this article can be found online at https://doi.org/10.1016/j.bbadis.2020.165900.

CRediT authorship contribution statement

Tanguy Demaret: Conceptualization, Data curation, Formal analysis, Funding acquisition, Methodology, Writing - original draft, Writing - review & editing. **Martin Roumain:** Conceptualization, Data curation, Formal analysis, Methodology, Writing - original draft,

Writing - review & editing. **Jérôme Ambroise:** Data curation, Formal analysis, Writing - original draft, Writing - review & editing. **Jonathan Evraerts:** Methodology, Writing - review & editing. **Joachim Ravau:** Methodology, Writing - review & editing. **Caroline Bouzin:** Methodology, Writing - review & editing. **Bertrand Bearzatto:** Methodology, Writing - review & editing. **Jean-Luc Gala:** Methodology, Writing - review & editing. **Hedwig Stepman:** Methodology, Writing - review & editing. **Sandrine Marie:** Methodology, Writing - review & editing. **Marie-Françoise Vincent:** Methodology, Writing - review & editing. **Giulio G. Muccioli:** Conceptualization, Writing - review & editing. **Mustapha Najimi:** Supervision, Writing - review & editing. **Etienne M. Sokal:** Conceptualization, Funding acquisition, Supervision, Writing - review & editing.

Declaration of competing interest

The authors declare that they have no known competing financial interests or personal relationships that could have appeared to influence the work reported in this paper.

Acknowledgments

The authors thank Michele de Beukelaer, Aurélie Daumerie, Tamah Abderrahman, Philippine Debeyne and Anniek Van Landschoot for excellent technical assistance. We are indebted to Pr Isabelle Leclercq for numerous pathological comments on liver slides, to Janne Tys for mouse embryonic fibroblasts isolation training, to Dr. Nicolas van Baren for fluorescent scanning expertise and to Pr Philippe Lysy who provided glucometer & strips.

Details of funding

Tanguy Demaret is a FRIA Grant Holder from the Fonds De La Recherche Scientifique - FNRS. The funding source had no involvement in the publication process.

Ethics approval

All experiments were carried out in accordance with the EU Directive 2010/63/EU for animal experiments and approved by the Ethical Committee for Animal Experimentation at the Health Science Sector, UCLouvain, Brussels, Belgium (2017/UCL/MD/006).

References

[1] E. Vasiljevic, Z. Ye, D.M. Pavelec, B.F. Darst, C.D. Engelman, M.W. Baker, Carrier frequency estimation of Zellweger spectrum disorder using ExAC database and bioinformatics tools, Genet. Med. 21 (9) (2019) 1969–1976.
[2] H.R. Waterham, S. Ferdinandusse, R.J. Wanders, Human disorders of peroxisome metabolism and biogenesis, Biochim. Biophys. Acta 1863 (2016) 922–933.
[3] F.C. Klouwer, K. Berendse, S. Ferdinandusse, R.J. Wanders, M. Engelen, B.T. Poll-The, Zellweger spectrum disorders: clinical overview and management approach, Orphanet journal of rare diseases 10 (2015) 151.
[4] K. Berendse, M. Engelen, S. Ferdinandusse, C.B. Majoie, H.R. Waterham, F.M. Vaz, J.H. Koelman, P.G. Barth, R.J. Wanders, B.T. Poll-The, Zellweger spectrum disorders: clinical manifestations in patients surviving into adulthood, J. Inherit. Metab. Dis. 39 (2016) 93–106.
[5] B.H. Vogel, S.E. Bradley, D.J. Adams, K. D'Aco, R.W. Erbe, C. Fong, A. Iglesias, D. Kronn, P. Levy, M. Morrissey, J. Orsini, P. Parton, J. Pellegrino, C.A. Saavedra-Matiz, N. Shur, M. Wasserstein, G.V. Raymond, M. Caggana, Newborn screening for X-linked adrenoleukodystrophy in New York State: diagnostic protocol, surveillance protocol and treatment guidelines, Mol. Genet. Metab. 114 (2015) 599–603.
[6] R.J. Wanders, F.C. Klouwer, S. Ferdinandusse, H.R. Waterham, B.T. Poll-The, Clinical and laboratory diagnosis of peroxisomal disorders, Methods in molecular biology (Clifton, N.J.), 1595 (2017) 329–342.
[7] H.R. Waterham, M.S. Ebberink, Genetics and molecular basis of human peroxisome biogenesis disorders, Biochim. Biophys. Acta 1822 (2012) 1430–1441.
[8] S.H. Korman, H. Mandel, A. Gutman, Characteristic urine organic acid profile in peroxisomal biogenesis disorders, J. Inherit. Metab. Dis. 23 (2000) 425–428.
[9] F. Rocchiccioli, P. Aubourg, P.F. Bougneres, Medium- and long-chain dicarboxylic aciduria in patients with Zellweger syndrome and neonatal adrenoleukodystrophy, Pediatr. Res. 20 (1986) 62–66.
[10] I. De Biase, S. Tortorelli, L. Kratz, J.S. S, K. Cusmano-Ozog, N. Braverman, Laboratory diagnosis of disorders of peroxisomal biogenesis and function: a technical standard of the American College of Medical Genetics and Genomics (ACMG), Genetics in medicine: official journal of the American College of Medical Genetics, (2019).
[11] N.E. Braverman, G.V. Raymond, W.B. Rizzo, A.B. Moser, M.E. Wilkinson, E.M. Stone, S.J. Steinberg, M.F. Wangler, E.T. Rush, J.G. Hacia, M. Bose, Peroxisome biogenesis disorders in the Zellweger spectrum: an overview of current diagnosis, clinical manifestations, and treatment guidelines, Mol. Genet. Metab. 117 (2016) 313–321.
[12] E.M. Sokal, F. Smets, A. Bourgois, L. Van Maldergem, J.P. Buts, R. Reding, J. Bernard Otte, V. Evrard, D. Latinne, M.F. Vincent, A. Moser, H.E. Soriano, Hepatocyte transplantation in a 4-year-old girl with peroxisomal biogenesis disease: technique, safety, and metabolic follow-up, Transplantation 76 (2003) 735–738.
[13] L. Van Maldergem, A.B. Moser, M.F. Vincent, D. Roland, R. Reding, J.B. Otte, R.J. Wanders, E. Sokal, Orthotopic liver transplantation from a living-related donor in an infant with a peroxisome biogenesis defect of the infantile Refsum disease type, J. Inherit. Metab. Dis. 28 (2005) 593–600.
[14] T. Demaret, S. Varma, X. Stephenne, F. Smets, I. Scheers, R. Wanders, L. Van Maldergem, R. Reding, E. Sokal, Living-donor liver transplantation for mild Zellweger spectrum disorder: up to 17 years follow-up, Pediatr. Transplant. 22 (3) (2018) e13112.
[15] M. Baes, P.P. Van Veldhoven, Mouse models for peroxisome biogenesis defects and beta-oxidation enzyme deficiencies, Biochim. Biophys. Acta 1822 (2012) 1489–1500.
[16] M. Baes, P. Gressens, E. Baumgart, P. Carmeliet, M. Casteels, M. Fransen, P. Evrard, D. Fahimi, P.E. Declercq, D. Collen, P.P. van Veldhoven, G.P. Mannaerts, A mouse model for Zellweger syndrome, Nat. Genet. 17 (1997) 49–57.
[17] P.L. Faust, M.E. Hatten, Targeted deletion of the PEX2 peroxisome assembly gene in mice provides a model for Zellweger syndrome, a human neuronal migration disorder, J. Cell Biol. 139 (1997) 1293–1305.
[18] M. Maxwell, J. Bjorkman, T. Nguyen, P. Sharp, J. Finnie, C. Paterson, I. Tonks, B.C. Paton, G.F. Kay, D.I. Crane, Pex13 inactivation in the mouse disrupts peroxisome biogenesis and leads to a Zellweger syndrome phenotype, Mol. Cell. Biol. 23 (2003) 5947–5957.
[19] A. Peeters, P. Fraisl, S. van den Berg, E. Ver Loren van Themaat, A. Van Kampen, M. H. Rider, H. Takemori, K.W. van Dijk, P.P. Van Veldhoven, P. Carmeliet, M. Baes, Carbohydrate metabolism is perturbed in peroxisome-deficient hepatocytes due to mitochondrial dysfunction, AMP-activated protein kinase (AMPK) activation, and peroxisome proliferator-activated receptor gamma coactivator 1alpha (PGC-1alpha) suppression, The Journal of biological chemistry, 286 (2011) 42162–42179.
[20] B.T. Poll-The, J. Gootjes, M. Duran, J.B. De Klerk, L.J. Wenniger-Prick, R.J. Admiraal, H.R. Waterham, R.J. Wanders, P.G. Barth, Peroxisome biogenesis disorders with prolonged survival: phenotypic expression in a cohort of 31 patients, American journal of medical genetics. Part A, 126a (2004) 333–338.
[21] K. Berendse, M. Boek, M. Gijbels, N.N. Van der Wel, F.C. Klouwer, M.A. van den Bergh-Weerman, A.B. Shinde, R. Ofman, B.T. Poll-The, S.M. Houten, M. Baes, R.J.A. Wanders, H.R. Waterham, Liver disease predominates in a mouse model for mild human Zellweger spectrum disorder, Biochimica et biophysica acta. Molecular basis of disease (2019).
[22] S. Hiebler, T. Masuda, J.G. Hacia, A.B. Moser, P.L. Faust, A. Liu, N. Chowdhury, N. Huang, A. Lauer, J. Bennett, P.A. Watkins, D.J. Zack, N.E. Braverman, G.V. Raymond, S.J. Steinberg, The Pex1-G844D mouse: a model for mild human Zellweger spectrum disorder, Mol. Genet. Metab. 111 (2014) 522–532.
[23] C. Argyriou, A. Polosa, B. Cecyre, M. Hsieh, E. Di Pietro, W. Cui, J.F. Bouchard, P. Lachapelle, N. Braverman, A longitudinal study of retinopathy in the PEX1-Gly844Asp mouse model for mild Zellweger spectrum disorder, Exp. Eye Res. 107713 (2019).
[24] G.E. Truett, P. Heeger, R.L. Mynatt, A.A. Truett, J.A. Walker, M.L. Warman, Preparation of PCR-quality mouse genomic DNA with hot sodium hydroxide and tris (HotSHOT), BioTechniques, 29 (2000) 52, 54.
[25] T. Fiebig, H. Boll, G. Figueiredo, H.U. Kerl, S. Nittka, C. Groden, M. Kramer, M.A. Brockmann, Three-dimensional in vivo imaging of the murine liver: a micro-computed tomography-based anatomical study, PLoS One 7 (2012) e31179.
[26] E.M. Sokal, J. Mostin, J.P. Buts, Liver metabolic zonation in rat biliary cirrhosis: distribution is reverse of that in toxic cirrhosis, Hepatology 15 (1992) 904–908.
[27] S. Orjuela, R. Huang, K.M. Hembach, M.D. Robinson, C. Soneson, ARMOR: an automated reproducible modular workflow for preprocessing and differential analysis of RNA-seq data, G3 (Bethesda, Md.), 9 (2019) 2089–2096.
[28] M.D. Robinson, D.J. McCarthy, G.K. Smyth, edgeR: a bioconductor package for differential expression analysis of digital gene expression data, Bioinformatics (Oxford, England), 26 (2010) 139–140.
[29] N. Aizarani, A. Saviano, Sagar, L. Mailly, S. Durand, J.S. Herman, P. Pessaux, T.F. Baumert, D. Grun, A human liver cell atlas reveals heterogeneity and epithelial progenitors, Nature, 572 (2019) 199–204.
[30] S.A. MacParland, J.C. Liu, X.Z. Ma, B.T. Innes, A.M. Bartczak, B.K. Gage, J. Manuel, N. Khuu, J. Echeverri, I. Linares, R. Gupta, M.L. Cheng, L.Y. Liu, D. Camat, S.W. Chung, R.K. Seliga, Z. Shao, E. Lee, S. Ogawa, M. Ogawa, M.D. Wilson, J.E. Fish, M. Selzner, A. Ghanekar, D. Grant, P. Greig, G. Sapisochin, N. Selzner, N. Winegarden, O. Adeyi, G. Keller, G.D. Bader, I.D. McGilvray, Single cell RNA sequencing of human liver reveals distinct intrahepatic macrophage populations, Nature communications, 9 (2018) 4383.
[31] R. Dobie, J.R. Wilson-Kanamori, B.E.P. Henderson, J.R. Smith, K.P. Matchett, J.R.

Portman, K. Wallenborg, S. Picelli, A. Zagorska, S.V. Pendem, T.E. Hudson, M.M. Wu, G.R. Budas, D.G. Breckenridge, E.M. Harrison, D.J. Mole, S.J. Wigmore, P. Ramachandran, C.P. Ponting, S.A. Teichmann, J.C. Marioni, N.C. Henderson, Single-cell transcriptomics uncovers zonation of function in the mesenchyme during liver fibrosis, Cell reports, 29 (2019) 1832–1847.e1838.

[32] M. Rakhshandehroo, G. Hooiveld, M. Muller, S. Kersten, Comparative analysis of gene regulation by the transcription factor PPARalpha between mouse and human, PLoS One 4 (2009) e6796.

[33] W. Huang, K. Ma, J. Zhang, M. Qatanani, J. Cuvillier, J. Liu, B. Dong, X. Huang, D.D. Moore, Nuclear receptor-dependent bile acid signaling is required for normal liver regeneration, Science 312 (2006) 233–236.

[34] T. Demaret, G.E. Courtoy, J. Ravau, P. Van Der Smissen, M. Najimi, E.M. Sokal, Accurate and live peroxisome biogenesis evaluation achieved by lentiviral expression of a green fluorescent protein fused to a peroxisome targeting signal 1, Histochem. Cell Biol. 153 (5) (2020) 295–306.

[35] M. De Rudder, C. Bouzin, M. Nachit, H. Louvegny, G. Vande Velde, Y. Jule, I.A. Leclercq, Automated computerized image analysis for the user-independent evaluation of disease severity in preclinical models of NAFLD/NASH, Laboratory investigation; a journal of technical methods and pathology, (2019).

[36] J.V. Passonneau, V.R. Lauderdale, A comparison of three methods of glycogen measurement in tissues, Anal. Biochem. 60 (1974) 405–412.

[37] P. Zhang, Analysis of mouse liver glycogen content, Bio-protocol 2 (2012) e186.

[38] N.V. Carroll, R.W. Longley, J.H. Roe, The determination of glycogen in liver and muscle by use of anthrone reagent, J. Biol. Chem. 220 (1956) 583–593.

[39] K. Sadilkova, S.M. Gospe Jr., S.H. Hahn, Simultaneous determination of alpha-aminoadipic semialdehyde, piperideine-6-carboxylate and pipecolic acid by LC-MS/MS for pyridoxine-dependent seizures and folinic acid-responsive seizures, J. Neurosci. Methods 184 (2009) 136–141.

[40] V. Mutemberezi, J. Masquelier, O. Guillemot-Legris, G.G. Muccioli, Development and validation of an HPLC-MS method for the simultaneous quantification of key oxysterols, endocannabinoids, and ceramides: variations in metabolic syndrome, Anal. Bioanal. Chem. 408 (2016) 733–745.

[41] O. Guillemot-Legris, V. Mutemberezi, P.D. Cani, G.G. Muccioli, Obesity is associated with changes in oxysterol metabolism and levels in mice liver, hypothalamus, adipose tissue and plasma, Sci. Rep. 6 (2016) 19694.

[42] M. Baes, P.P. Van Veldhoven, Hepatic dysfunction in peroxisomal disorders, Biochim. Biophys. Acta 1863 (2016) 956–970.

[43] S. Goldfischer, C.L. Moore, A.B. Johnson, A.J. Spiro, M.P. Valsamis, H.K. Wisniewski, R.H. Ritch, W.T. Norton, I. Rapin, L.M. Gartner, Peroxisomal and mitochondrial defects in the cerebro-hepato-renal syndrome, Science 182 (1973) 62–64.

[44] J.M. Scotto, M. Hadchouel, M. Odievre, M.H. Laudat, J.M. Saudubray, O. Dulac, I. Beucler, P. Beaune, Infantile phytanic acid storage disease, a possible variant of Refsum's disease: three cases, including ultrastructural studies of the liver, J. Inherit. Metab. Dis. 5 (1982) 83–90.

[45] M.F. Wangler, Y.H. Chao, V. Bayat, N. Giagtzoglou, A.B. Shinde, N. Putluri, C. Coarfa, T. Donti, B.H. Graham, J.E. Faust, J.A. McNew, A. Moser, M. Sardiello, M. Baes, H.J. Bellen, Peroxisomal biogenesis is genetically and biochemically linked to carbohydrate metabolism in Drosophila and mouse, PLoS Genet. 13 (2017) e1006825.

[46] N.E. Braverman, A.B. Moser, Functions of plasmalogen lipids in health and disease, Biochim. Biophys. Acta 1822 (2012) 1442–1452.

[47] K. Wiens, S.A. Berry, H. Choi, A. Gaviglio, A. Gupta, A. Hietala, D. Kenney-Jung, T. Lund, W. Miller, E.I. Pierpont, G. Raymond, H. Winslow, H.A. Zierhut, P.J. Orchard, A report on state-wide implementation of newborn screening for X-linked Adrenoleukodystrophy, Am. J. Med. Genet. A 179 (2019) 1205–1213.

[48] F.C.C. Klouwer, S. Ferdinandusse, H. van Lenthe, W. Kulik, R.J.A. Wanders, B.T. Poll-The, H.R. Waterham, F.M. Vaz, Evaluation of C26:0-lysophosphatidylcholine and C26:0-carnitine as diagnostic markers for Zellweger spectrum disorders, J. Inherit. Metab. Dis. 40 (6) (2017) 875–881.

[49] R.J. Wanders, H.R. Waterham, Biochemistry of mammalian peroxisomes revisited, Annu. Rev. Biochem. 75 (2006) 295–332.

[50] S. Ferdinandusse, S. Denis, P.L. Faust, R.J. Wanders, Bile acids: the role of peroxisomes, J. Lipid Res. 50 (2009) 2139–2147.

[51] Y. Gielchinsky, N. Laufer, E. Weitman, R. Abramovitch, Z. Granot, Y. Bergman, E. Pikarsky, Pregnancy restores the regenerative capacity of the aged liver via activation of an mTORC1-controlled hyperplasia/hypertrophy switch, Genes Dev. 24 (2010) 543–548.

[52] I. Matot, N. Nachmansson, O. Duev, S. Schulz, K. Schroeder-Stein, S. Frede, R. Abramovitch, Impaired liver regeneration after hepatectomy and bleeding is associated with a shift from hepatocyte proliferation to hypertrophy, FASEB journal: official publication of the Federation of American Societies for Experimental Biology 31 (2017) 5283–5295.

[53] Z. Shi, A.E. Wakil, D.C. Rockey, Strain-specific differences in mouse hepatic wound healing are mediated by divergent T helper cytokine responses, Proc. Natl. Acad. Sci. U. S. A. 94 (1997) 10663–10668.

[54] S. Hillebrandt, C. Goos, S. Matern, F. Lammert, Genome-wide analysis of hepatic fibrosis in inbred mice identifies the susceptibility locus Hfib1 on chromosome 15, Gastroenterology 123 (2002) 2041–2051.

[55] P.L. Faust, Abnormal cerebellar histogenesis in PEX2 Zellweger mice reflects multiple neuronal defects induced by peroxisome deficiency, J. Comp. Neurol. 461 (2003) 394–413.

[56] P.L. Faust, W.J. Kovacs, Cholesterol biosynthesis and ER stress in peroxisome deficiency, Biochimie 98 (2014) 75–85.

[57] W.J. Kovacs, J.E. Shackelford, K.N. Tape, M.J. Richards, P.L. Faust, S.J. Fliesler, S.K. Krisans, Disturbed cholesterol homeostasis in a peroxisome-deficient PEX2 knockout mouse model, Mol. Cell. Biol. 24 (2004) 1–13.

[58] W.J. Kovacs, K.N. Tape, J.E. Shackelford, T.M. Wikander, M.J. Richards, S.J. Fliesler, S.K. Krisans, P.L. Faust, Peroxisome deficiency causes a complex phenotype because of hepatic SREBP/Insig dysregulation associated with endoplasmic reticulum stress, J. Biol. Chem. 284 (2009) 7232–7245.

[59] M. Matsunami, N. Shimozawa, A. Fukuda, T. Kumagai, M. Kubota, P.F. Chong, M. Kasahara, Living-donor liver transplantation from a heterozygous parent for infantile Refsum disease, Pediatrics, 137, (2016).

[60] K. Berendse, B.G.P. Koot, F.C.C. Klouwer, M. Engelen, F. Roels, M.M. Lacle, P.G.J. Nikkels, J. Verheij, B.T. Poll-The, Hepatic symptoms and histology in 13 patients with a Zellweger spectrum disorder, J. Inherit. Metab. Dis. 42 (5) (2019) 955–965.

[61] A. Janssen, P. Gressens, M. Grabenbauer, E. Baumgart, A. Schad, I. Vanhorebeek, A. Brouwers, P.E. Declercq, D. Fahimi, P. Evrard, L. Schoonjans, D. Collen, P. Carmeliet, G. Mannaerts, P. Van Veldhoven, M. Baes, Neuronal migration depends on intact peroxisomal function in brain and in extraneuronal tissues, J. Neurosci. 23 (2003) 9732–9741.